FINAL TECHNICAL REPORT

For United States Geological Survey

National Earthquake Hazards Reduction Program

External Research Grant

Project Award: 04-HQGR-0119

SPACE GEODETIC CONSTRAINTS ON FAULT SLIP RATES AND THE DISTRIBUTION OF ASEISMIC SLIP ON BAY AREA FAULTS

Principal investigator:

Roland Bürgmann

University of California, Berkeley
Department of Earth and Planetary Science
307 McCone Hall
Berkeley, CA 94720-4767
Telephone: (510) 643-9545;
Fax:(510) 643-9980;
e-mail: burgmann@seismo.berkeley.edu

Space geodetic constraints on fault slip rates and the distribution of aseismic slip on Bay Area faults

Roland Bürgmann
University of California, Berkeley
Department of Earth and Planetary Science
307 McCone Hall
Berkeley, CA 94720-4767
Telephone: (510) 643-9545;
Fax:(510) 643-9980;
e-mail: burgmann@seismo.berkeley.edu

Award Number: 04-HQGR-0119

1.1 Abstract

This project addresses the seismic potential and natural hazard presented by major strike-slip and associated thrust faults in the San Francisco Bay Area through the use of space geodesy, namely GPS surface velocities. Geodetic measurements provide information on the magnitude of elastic strain accumulation about seismogenic faults, their locking depth and slip rates, the distribution of subsurface aseismic fault slip on a subset of those faults, and any variations of those parameters in space and time. Observations of surface deformation allow us to determine the kinematics of faults in the San Francisco Bay Area. We present the Bay Area Velocity Unification (BAVU, "Bay-View"), a new compilation of over 200 horizontal surface velocities computed from campaign-style and continuous Global Positioning System (GPS) observations from 1993-2003. We interpret this interseismic velocity field using a 3-D block model to determine the relative contributions of block motion, elastic strain accumulation, and shallow aseismic creep. The total relative motion between the Pacific plate and the rigid Sierra Nevada/Great Valley (SNGV) microplate is 37.9 ± 0.6 $mm \cdot yr^{-1}$ directed towards N 30.4°W ±0.8° at the latitude of San Francisco. Fault slip rates from our preferred model are generally in agreement with geologic estimates. The strike-slip rate on the San Gregorio fault of 2.4 ± 0.5

$mm \cdot yr^{-1}$ is constrained by global stations from throughout the Pacific plate as well as local Bay Area stations. We find notable slip on two faults that have not been previously discussed in great detail, both indicative of substantial slip east of the central Bay Area: the West Napa fault ($4.0 \pm 3.0\ mm \cdot yr^{-1}$) and a fault or zone of faulting along the eastern margin of the Coast Range ($5.4 \pm 1.0\ mm \cdot yr^{-1}$). We find that the Mount Diablo thrust system allows slip to transfer from the Greenville fault to the Concord/Green Valley fault system, and accommodates $3.9 \pm 0.5\ mm \cdot yr^{-1}$ of reverse-slip as well as $4.2 \pm 0.5\ mm \cdot yr^{-1}$ of right-lateral strike-slip. Geodetic data permit slip on the northern Calaveras to step either west or east, with our preferred model including slip being partitioned between both the West Napa and Concord/Green Valley fault systems. We resolve $< 3\ mm \cdot yr^{-1}$ of convergence perpendicular to the mapped strike of faults along the eastern margin of the Coast Range, but this is balanced by almost equal amounts of extension west of the Bay in our models such that the total convergence across the Bay Area is negligible. The poles of rotation for blocks within the Bay Area are located between the North America-Pacific and North America-SNGV poles, with a progression from west to east. The orientation of present-day relative plate motion cannot explain the strike of most Bay Area faults, but fault strike does loosely correlate with inferred plate motions at the time each fault initiated.

1.2 Introduction

The San Francisco Bay Area hosts a complex plate boundary fault system with large, seismogenic faults that pose a significant hazard to the local urban population. Faults in the Bay Area are predominantly locked at the surface while steady plate-boundary motion continues to deform the surrounding crust. Monitoring this surface deformation allows us to determine block offset and strain accumulation along the faults. Geodetic monitoring of faults in the Bay Area has been a major effort of the scientific community since Reid first formulated the elastic rebound theory [*Reid*, 1910]. The development of modern survey techniques such as the Global Positioning System (GPS) allows enhanced measurement precision. A number of studies have reported the results of GPS deformation fields and their estimates of the slip distribution on Bay Area faults [*Savage et al.*, 1998; *Freymueller et al.*, 1999; *Savage et al.*, 1999; *Murray and Segall*, 2001; *Prescott et al.*, 2001]. Studies have also used combinations of GPS and terrestrial geodetic measurements to determine distribution of aseismic creep at depth on the Hayward [*Bürgmann et al.*, 2000; *Simpson et al.*, 2001; *Malservisi et al.*, 2003; *Schmidt et al.*, 2004] and Calaveras [*Manaker et al.*, 2003] faults. While most of these studies assume that deformation occurs at a constant rate over the period of observation, a few geodetic studies focus on transient deformation. Such transients include coseismic offset in the 1868 Hayward fault earthquake [*Yu and Segall*, 1996], the 1906 San Andreas fault earthquake [*Thatcher et al.*, 1997], and the 1989 Loma Prieta earthquake near the San Andreas fault [*Arnadottir and Segall*, 1994, 1996]. Postseismic deformation has been described for the 1906 earthquake [*Thatcher*, 1975; *Kenner and Segall*, 2000] and for transient effects of the 1989 earthquake near the San Andreas [*Bürgmann et al.*, 1997] and Hayward [*Lienkaemper et al.*, 1997, 2001] faults. Through all these efforts, we have begun to understand the detailed slip distribution of Bay Area faults. Each new study

brings higher precision data and more sophisticated modeling techniques employing fewer simplifying assumptions.

We present a compilation of GPS measurements for the Bay Area showing the interseismic velocity field from 1993-2003. We then interpret these velocities using a three-dimensional block model that considers the motion of regional crustal blocks and elastic strain accumulation about block-bounding faults. This modeling effort relaxes many simplifying assumptions used in previous studies regarding fault geometry, spherical earth effects and also allows for fault perpendicular motion. We evaluate deformation at a range of scales including global tectonics, Bay Area wide deformation, and the details of fault geometry and connections on the scale of kilometers.

1.3 GPS Data and Processing

1.3.1 Data Collection

The Bay Area Velocity Unification (BĀVŪ, pronounced "Bay-View") includes campaign GPS data collected by six different institutions (U.C. Berkeley; U.S.G.S.; Stanford; U.C. Davis; U. Alaska, Fairbanks; CalTrans) over a decade from 1993 - 2003. Transient deformation from the 1989 Loma Prieta Earthquake decayed to near zero by 1993 [*Segall et al.*, 2000], so this time period should capture relatively steady interseismic strain accumulation.

At U. C. Berkeley we occupy each benchmark in our campaign GPS networks yearly. UNAVCO archives all of our raw data online (http://archive.unavco.org). When possible, we collect data for at least two continuous 24-hour sessions, with some occupations spanning as long as seven days. However, much of the study area is in urban or suburban settings, making it impossible to leave GPS equipment unattended. These concerns limit the occupation time to the logistical limits of the human operator. For these sites, occupations may be as short as 6 hours or as long as 12 hours, depending upon the time it takes to travel to the site and the efficiency of the operator. We frequently repeat surveys of these sites for a total of two observations during each year. Other agencies contributing data to the BĀVŪ dataset generally follow the same guidelines and provide at least 6 hours of data per site per day, however a substantial portion of the CalTrans data is limitted to 3 hours or less.

1.3.2 GPS Processing

We process campaign GPS data using the GAMIT/GLOBK software package developed at the Massachusetts Institute of Technology [*King and Bock*, 2002; *Herring*, 2002], which uses double-difference phase observations to determine baseline distances and orientations between ground-based GPS receivers. Along with campaign data, we include five global stations from the International GPS Service (IGS) network and four to six nearby continuous stations from the BARD network in our processing runs.

Table 1.1. Global GPS stations included in modeling of stable North America and Pacific plates.

Pacific (6)	CHAT KOKB KWJ1 MKEA TAHI THTI
North America (26)	ALGO AMC2 AOML BARN BRMU CHUR DUBO FAIR FLIN GODE KELY MDO1 MIA3 NLIB NRC1 PIE1 PRDS RCM5 RCM6 SCH2 STJO THU1 USNO WES2 WHIT YELL

We combine daily ambiguity-fixed, loosely constrained solutions using the Kalman filter approach implemented by GLOBK [*Herring*, 2002]. We include data processed locally as well as solutions for the full IGS and BARD networks processed by and obtained from SOPAC at the Scripps Oceanographic Institute of U.C. San Diego. Using the Kalman filter, we combine all daily solutions to generate an average solution for each month, giving each observation equal weight. We then estimate the average linear velocity of each station in the network from these monthly files. We fix the final positions and velocities of the IGS stations into the ITRF2000 No Net Rotation global reference frame [*Altamimi et al.*, 2002] using the GLORG stabilization routine, allowing for rotation and translation of the network. The stations we use to define the reference frame are listed in Table 1.1. We scale the errors following the method used by the Southern California Earthquake Center's Crustal Motion Map version 3.0 team [SCEC CMM 3.0; Robert W. King, pers. comm., 2003]. We add white noise to the formal uncertainties of all stations with a magnitude of 2 $mm \cdot yr^{-1}$ for the horizontal components and 5 $mm \cdot yr^{-1}$ for the vertical component. To account for "benchmark wobble," we add Markov process noise to the solutions with a magnitude of 1 $mm \cdot yr^{-\frac{1}{2}}$. We also include select velocities from SCEC CMM 3.0 [*Shen et al.*, 2003] in the Parkfield area to provide better coverage in central California.

We show the BĀVŪ GPS data for the Bay Area in Fig. 1.1 (also Table ES1*). We prefer to visualize velocities in a local reference frame centered around station LUTZ (a BARD continuous site on the Bay Block, roughly at the BĀVŪ network centroid). It accentuates the gradient in deformation across the Bay Area and allows easy visual identification of the differences between stations. We subtract LUTZ's ITRF2000 velocity from all stations and propagate the correlations in uncertainty to get the error ellipses.

1.3.3 No Outlier Exclusion

We include velocities for all stations that have at least four total observations spanning at least three years. At no point during the data processing or modeling do we exclude data that appear to be "outliers" based on initial assumptions about plate boundary motion or

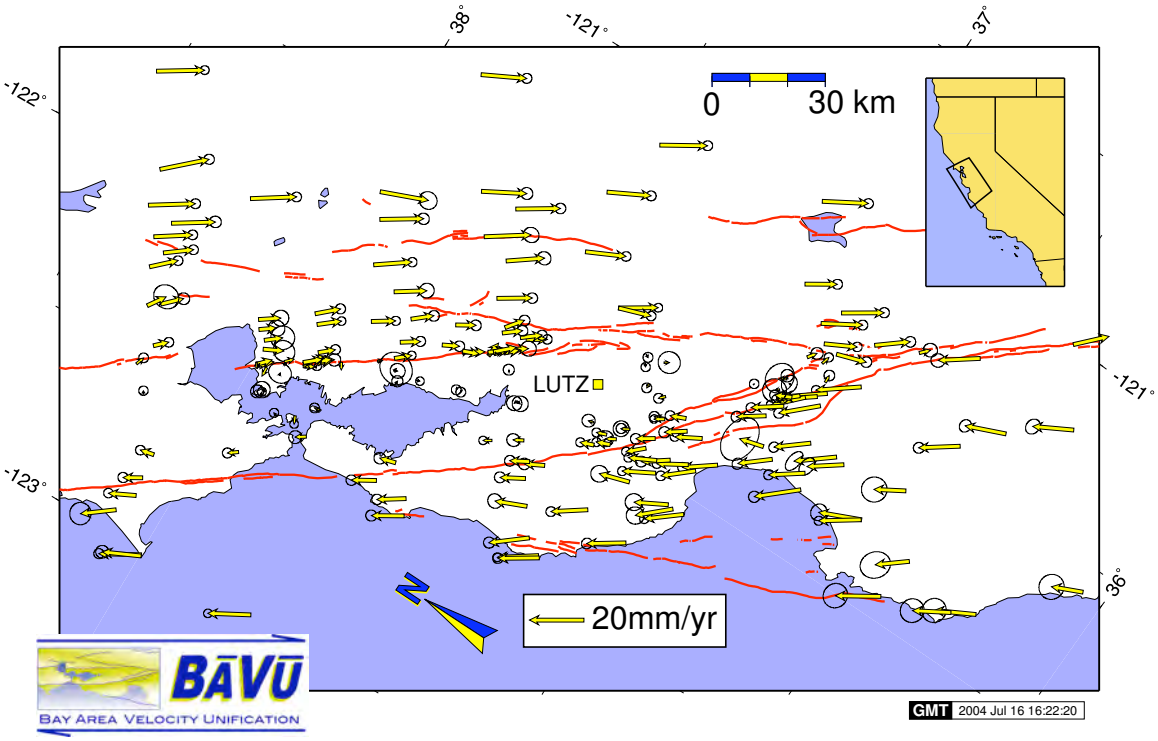

Figure 1.1. The BĀVŪ data set. Map of the San Francisco Bay Area with GPS Velocities from 1994-2003 relative to station LUTZ in the Bay Block. The map projection is about the Pacific Plate–Sierra Nevada/Great Valley (PA-SNGV) pole of rotation, so velocities along a small circle path predicted from the rotation axis of the PA-SNGV block rotation show up as horizontal vectors.

model misfit. This ensures that the data truly dictate the model results, and that scatter in the data is treated formally.

1.4 Block Modeling Methodology

In order to calculate slip along faults at depth from observed surface deformation, we must employ interpretive models. In the following sections, we discuss the physical processes that are represented in our numerical model, including block offset, elastic strain accumulation, and shallow interseismic creep.

1.4.1 Dislocation modeling

The San Andreas fault system forms the boundary between the Pacific (PA) plate and the Sierra Nevada/Great Valley block (SNGV). Far from the fault, plate tectonic motions continue at a relatively constant rate. In the Bay Area, faults are presently locked near the surface, causing the entire region to deform elastically under the influence of this far-field plate motion. One parallel way of representing this system is to imagine that the fault itself is locked near the surface, but continues to slip at depth. *Okada* [1985] presents a useful formulation of the mathematics of this relationship for finite fault segments ("dislocations") in an isotropic, homogeneous, linearly elastic half space. An essential assumption in dislocation modeling is that we can represent the steady long-term motion between two blocks of crust as deep slip on a discrete elastic dislocation at the boundary between the blocks. While there are a variety of other approaches to the problem, *Gilbert et al.* [1994] support this assumption with the observation that strain accumulation axes are parallel to local fault strikes rather than far-field plate motion. Models also show that geodetic data can be treated in this manner because they are insensitive to the details of the processes driving plate tectonics [*Savage*, 1990, 2000]. We therefore treat the terms "long-term" slip rate and "deep" slip rate for a fault as synonyms. While fault slip rates can be influenced by local stress perturbations from earthquakes or change over geologic time, we make the simplifying assumption that these rates are constant during the decade spanned by the BĀVŪ data set.

Okada's equations define the relationship between slip on a given fault segment and surface displacement at each station. The equations can be used to calculate a Green's function for the inverse problem to solve for the slip rate most consistent with the data when fault geometry is assumed. To uniquely define the Green's function, one must specify the depth at which the fault transitions from the locked behavior near the surface to the deep, continuously slipping dislocation representing the boundary condition of long-term plate motion. The transition could reflect thermally controlled onset of plastic flow [*Sibson*, 1982] or the transition from stable to unstable frictional sliding [*Tse and Rice*, 1986; *Blanpied et al.*, 1995]. Below the transition, rocks can actively deform by plastic creep. For geodetic modeling, this transition is often called the "locking depth" (LD). Dislocation models usually solve for a uniform slip rate at all depths below LD, but the transition in

reality may occur gradually over a wider zone. To account for the fact that a fault may not be completely locked at all depths above the transition, additional finite dislocations can be added to an inversion, each with a uniform slip rate covering a patch of the fault surface.

The fault segments in dislocation modeling are mathematically independent of one another and the best statistical fit to the data frequently juxtaposes segments with unrealistically high slip and very low slip. Since such strong slip heterogeneity would require very high stress concentrations, it is considered physically unreasonable and spatial smoothing is often applied to stabilize the results. The exact smoothing parameters chosen can alter the inferred peak slip and distribution of slip – sometimes changing the character and interpretation of the results [e.g., *Segall and Harris*, 1987].

1.4.2 Block Modeling

Block modeling is an extension of dislocation modeling, but instead of allowing each segment to be independent, we add the additional physical constraint that dislocations form the boundaries of rigid plates, or "blocks" [e.g., *Bennett et al.*, 1996; *Murray and Segall*, 2001; *McCaffrey*, 2002]. The amount of slip along each dislocation must therefore be consistent with the motion of the entire block, resulting in continuity of slip on adjacent fault segments without a positivity constraint or artificial smoothing. Here we use an extension of the block modeling code by *Meade et al.* [2002, , also has a concise introduction to block modeling] and *Meade and Hager* [2004, , latest formulation of the methodology].

In block modeling, we define blocks on a spherical earth (analogous to plates) bounded by faults. Defining the model geometry therefore requires more information than dislocation modeling because the location of fault connections must be known so that the faults form a continuous boundary around every block (Section 1.4.4). Each block rotates about a "rotation axis" passing through the center of the earth and intersecting the surface at a "pole of rotation" (sometimes referred to as an "Euler pole", *Cox and Hart* [1986]). The motion of individual points on a block is a result of the rigid rotation of that block plus elastic deformation due to locking of faults at the block boundaries. The motion satisfies:

$$\mathbf{v}(\mathbf{r}_i) = \mathbf{\Omega}_i \times \mathbf{r}_i - \sum_{f=1}^{\#Faults} \mathbf{G}_i^f \cdot \mathbf{s}^f \tag{1.1}$$

where $\mathbf{r}_i$ is the position of station i on earth, $\mathbf{v}$ is the predicted velocity, the first term on the right side (cross product term) represents rigid rotation about an axis passing through the center of the earth, and the second term (summation term) represents elastic strain related to fault slip on each segment. $\mathbf{\Omega}_i$ is the vector representing the rotation axis for the block on which station i lies. The magnitude of elastic deformation at a point is determined by the Green's function $\mathbf{G}$, relating unit slip on fault f to the effect on station i, times the actual magnitude of slip on that fault, $\mathbf{s}^f$. Our implementation of the block model utilizes what is often referred to as the "backslip" approach to implementing strain accumulation. Essentially, strain accumulation on a fault driven by a deep dislocation that extends from the locking depth to infinite depth is mathematically equivalent to a rigid block offset plus slip on the fault between the surface and the locking depth of opposite slip sense. While this

approach avoids implementing dislocations that extend to infinite depths, it assumes that the fault geometry is planar from the surface to infinite depths and causes some limitations to the block geometry that we can implement. As a result, we primarily use vertical fault segments in our model (see Section 1.6.2).

Equation 1.1 includes both $\mathbf{\Omega}$ and $\mathbf{s}$ as unknown parameters. However, the slip rate of block bounding faults is a directly determined by the relative rotation of the surrounding blocks. We can express the magnitude and azimuth of relative motion that must be accomodated along each block boundary as a function of the rotation axes. We resolve this relative motion onto the orientation of the fault that accomodates the motion, and the ratio between strike-slip and dip-slip components is controlled exclusively by the fault orientation ($\mathbf{s} = f(\mathbf{\Omega}$, fault strike, fault dip). Because of this relationship, we replace $\mathbf{G}_i^f \cdot \mathbf{s}^f$ in Eq. 1.1 with $\mathbf{J}_i^f \cdot \mathbf{\Omega}_i$, where $\mathbf{J}$ is a matrix of partial derivatives relating a unit rotation of each component of $\mathbf{\Omega}$ to surface deformation from strain accumulation along block-bounding faults. Thus for each block in the model, there are only three unknown parameters – the three components of $\mathbf{\Omega}$. We solve this modified equation in an inverse sense where we know $\mathbf{v}$ and we solve for the $\mathbf{\Omega}$ most consistent with these observed velocities.

1.4.3 Inclusion of Global Data

All stations on a given block contribute to the estimated rotation axis. We are therefore able to incorporate data from throughout the Pacific (PA) and North American (NA) plates to determine the total magnitude of relative motion that must be accommodated by Bay Area faults. As long as the assumption that the plates behave rigidly in their interiors is valid, global data far from faults provide valuable constraints. (Strictly speaking, we treat the blocks as purely elastic. Because the blocks are so large, points near the plate interior are virtually unaffected by elastic strain at the block boundaries. Hence, we refer to block interiors as "rigid.") However, it is not our goal to estimate all global plate motions. Other than the blocks defined within the Bay Area, we only include data and define block boundaries for the PA,NA, and SNGV plates so that we are not biased by uncertainties in the motion of other global plates outside our area of interest. Figure 1.2 shows the distribution of global stations that we use.

Our block geometry includes a boundary between the SNGV and North American plates along the Eastern California Shear Zone (ECSZ) (Fig. 1.3). We exclude sites GOLD and GOL2 from our modeling because they are within the ECSZ and affected by complex local fault geometry that is not within our area of interest [*McClusky et al.*, 2001]. While the SNGV block is thought to behave rigidly [*Argus and Gordon*, 1991], the Basin and Range between eastern California and the Colorado Plateau is an area of distributed deformation [*Thatcher et al.*, 1999; *Bennett et al.*, 2003]. We do not include data from within the Basin and Range, so we are insensitive to the details of how deformation is distributed across it. Our ECSZ boundary is therefore a proxy for the total deformation in the Basin and Range between the SNGV and stable North America.

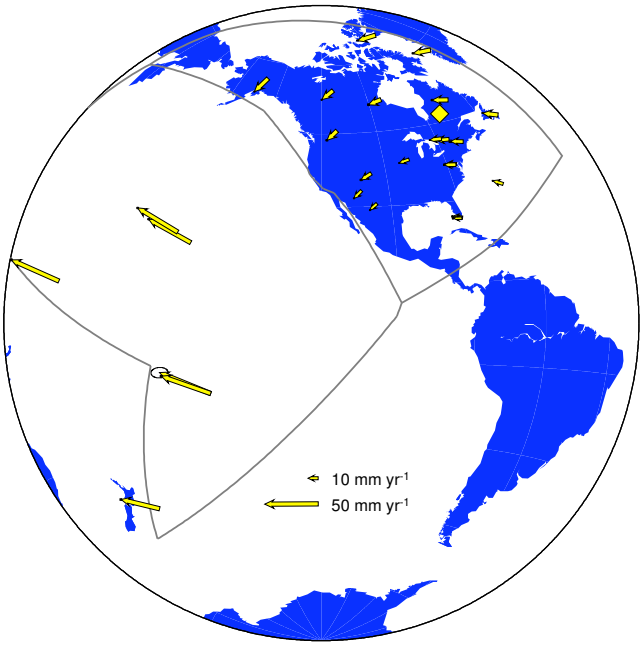

Figure 1.2. Observed global GPS velocities shown in ITRF2000 No Net Rotation (NNR) reference frame. Figure shows only stations included in modeling, but BĀVŪ includes additional global stations from reference frame stabilization. We transform the data into a stable North America reference frame for modeling.

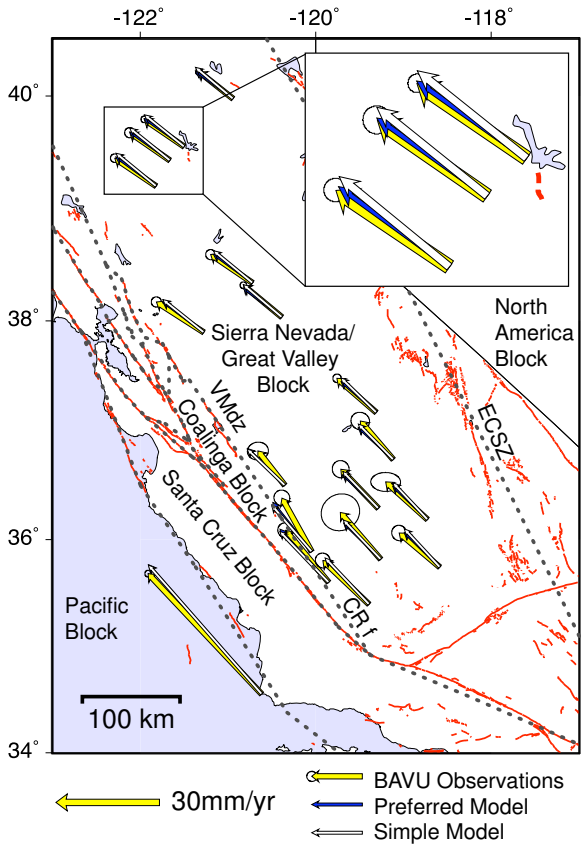

Figure 1.3. GPS observations within California, shown in a reference frame with stable north America (wide vectors with error ellipses) compared with model results (narrow vectors). Dark sinuous lines are Holocene active faults. Dotted grey lines show a representative model geometry from our Complex model that includes all segments. We label select blocks and faults outside the Bay Area. VMdz = Valley Margin deformation zone; ECSZ = Eastern California Shear Zone. The inset shows an enlargement of the area where the two models differ most in the northern section of the figure. Our Preferred model with a Valley Margin deformation zone (darker vectors) fit the data better than models that exclude this fault (Simple model, white vectors).

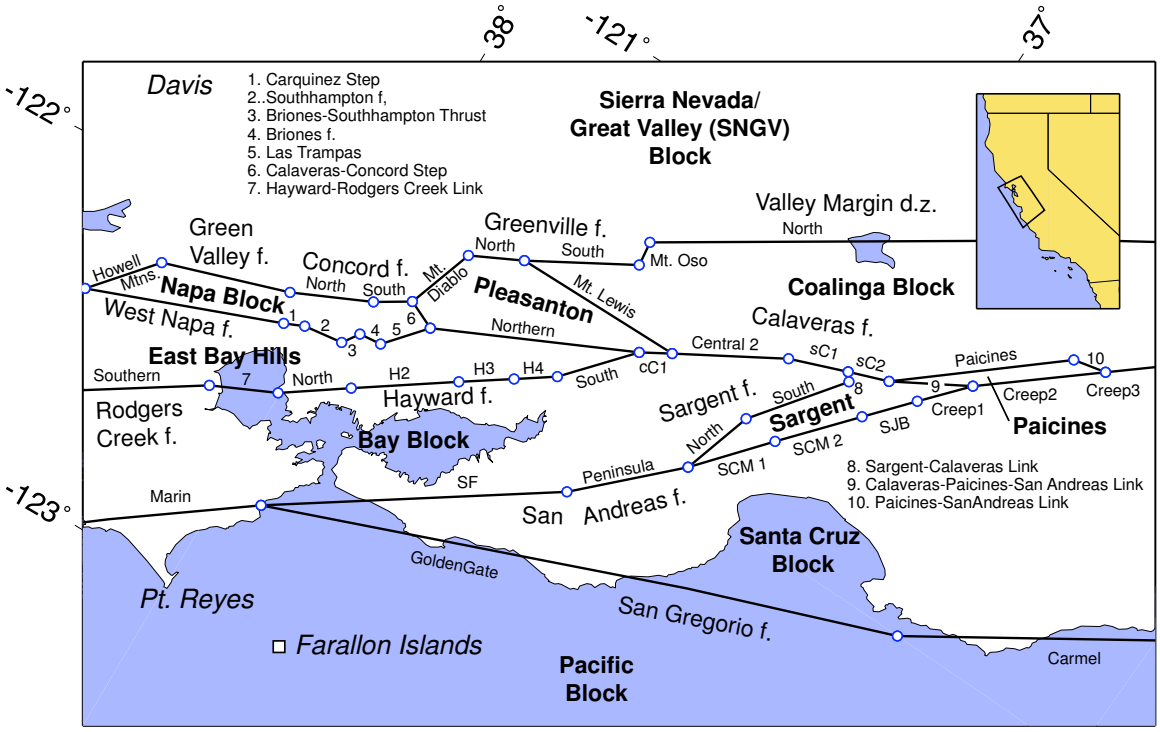

Figure 1.4. Model fault segments in the Bay Area. Note that not all segments are used in all model variations. Block names in large, bold text. Fault names in larger plain text and names of sub-segments of those faults in smaller text. Place names in italics. Abbreviations: cC = central Calaveras; sC = southern Calaveras; SF = San Francisco; SCM = Santa Cruz Mountains; SJB = San Juan Bautista; f. = fault. See also Table 1.2.

1.4.4 Fault Geometry

The geometry of faults, particularly in the presence of branching faults, can have a dramatic effect on the distribution of slip between them [e.g., *d'Alessio and Martel*, 2004]. With block-modeling, we face a difficult challenge in defining the precise fault geometry, especially at fault branches and other connections which are not well defined in the Bay Area. Recent geologic and geomorphic mapping efforts throughout the Bay Area, and especially in the northern East Bay Area, provide new constraints on the details of fault geometry [Jeff Unruh, pers. comm., 2004]. We define faults in our model using a combination of several data types: 1) Mapped surface traces of faults; 2) Relocated microseismicity; 3) Topographic lineaments; and 4) Interpreted geologic cross sections.

We have explored dozens of variations on model geometry including a wide range of complexities. Our goals are to determine the simplest model that explains the data and test competing model geometries to determine if they are consistent with the geodetic data. Figure 1.4 and Table 1.2 show model fault segments presented in this manuscript and Table 1.3 describes the variations we discuss. We include models that range in complexity

Table 1.2. Definition of model geometry. Fault systems are listed from west to east, with individual fault segments listed from north to south. Columns 2 - 5 show longitude (Lon) and latitude (Lat) of starting and ending points of each segment. LD = Locking depth, based on D_{95}. LD of zero indicates only block motion across a segment with no strain accummulation. Such faults are either known to be creeping (central San Andreas) or are short connecting segments with unknown geometry. Creep column indicates the *a priori* constraint and 1σ bounds placed on the shallow slip rate (uniform rate from the surface to the locking depth). If no rate is given, we assume the fault is locked above LD and do not solve for shallow slip on that segment. Last column indicates model geometries in which the segment appears: S = Simple; P= Preferred; C=Complex.

Name	**Lon**$_{start}$ °E	**Lat**$_{start}$ °N	**Lon**$_{end}$ °E	**Lat**$_{end}$ °N	L.D. km	**Creep** $mm \cdot yr^{-1}$	**Models**
SanGregorio_GoldenGate	-122.673	37.905	-122.000	36.501	13	–	SPC
SanGregorio_CarmelSouth	-122.000	36.501	-121.375	35.750	14	–	SPC
SanAndreas_Mendocino	-124.241	40.264	-123.690	38.999	15	–	SPC
SanAndreas_Marin	-123.690	38.999	-122.673	37.905	15	–	SPC
SanAndreas_SF	-122.673	37.905	-122.174	37.324	12	–	SPC
SanAndreas_Peninsula	-122.174	37.324	-121.926	37.120	14	–	SPC
SanAndreas_SantaCruzMountains1	-121.926	37.120	-121.729	36.985	15	–	SPC
SanAndreas_SantaCruzMountains2	-121.729	36.985	-121.533	36.850	15	[a]	SPC
SanAndreas_SanJuanBautista	-121.533	36.850	-121.409	36.765	10	14.0 ± 2.0	SPC
SanAndreas_Creep1	-121.409	36.765	-121.286	36.679	0	–	SPC
SanAndreas_Creep2	-121.286	36.679	-121.042	36.448	0	–	SPC
SanAndreas_Creep3	-121.042	36.448	-120.614	36.052	0	–	SPC
SanAndreas_ParkfieldTransition	-120.614	36.052	-120.359	35.814	10	–	SPC
RodgersCreek_North	-123.551	39.756	-122.979	38.810	10	–	SPC
RodgersCreek_South	-122.979	38.810	-122.450	38.147	10	–	SPC
HaywardRodgersCreekStepover	-122.450	38.147	-122.368	38.004	0	–	SPC
Hayward_North	-122.368	38.004	-122.247	37.867	10	4.6 ± 0.5	SPC
Hayward_2	-122.247	37.867	-122.070	37.666	12	3.6 ± 0.5	SPC
Hayward_3	-122.070	37.666	-121.980	37.563	11	5.2 ± 0.3	SPC
Hayward_4	-121.980	37.563	-121.909	37.482	11	4.4 ± 0.5	SPC
Hayward_South	-121.909	37.482	-121.725	37.355	10	–	SPC
WestNapa	-122.389	38.501	-122.188	38.074	11	–	SPC
Calaveras_CarquinezStepover	-122.188	38.074	-122.164	38.030	11	–	PC
SouthHampton	-122.164	38.030	-122.149	37.939	12	–	PC
BrionesSouthHamptonThrust	-122.149	37.939	-122.102	37.914	12	–	PC
Briones	-122.102	37.914	-122.095	37.862	12	–	PC
LasTrampas	-122.095	37.862	-121.982	37.785	12	–	PC
Calaveras_Northern	-121.982	37.785	-121.725	37.355	12	3.0 ± 0.8	SPC
Calaveras_Central1	-121.725	37.355	-121.677	37.290	9	9.4 ± 2.0	SPC
Calaveras_Central2	-121.677	37.290	-121.510	37.062	9	14.0 ± 0.2[b]	SPC
Calaveras_Southern1	-121.510	37.062	-121.449	36.933	9	10.6 ± 2.0	SPC
Calaveras_Southern2	-121.449	36.933	-121.407	36.843	9	10.6 ± 2.0	SPC
GreenValley_HowellMtns	-122.389	38.501	-122.215	38.380	0	–	SPC
GreenValley	-122.215	38.380	-122.102	38.098	11	4.4 ± 0.4	SPC
Concord_North	-122.102	38.098	-122.003	37.925	16	3.6 ± 0.3	SPC
Concord_South	-122.003	37.925	-121.944	37.851	16	2.7 ± 0.3	SPC
Calavaras_ConcordStep	-121.982	37.785	-121.944	37.851	15	–	SPC
MtDiabloThrust	-121.944	37.851	-121.749	37.797	17	–	SPC
Greenville_North	-121.749	37.797	-121.678	37.684	18	–	SPC
Greenville_South	-121.678	37.684	-121.516	37.460	18	–	PC
MtOsoAnticline	-121.516	37.460	-121.445	37.467	18	–	PC
ValleyMargin_North	-121.445	37.467	-120.398	36.202	18	–	PC
ValleyMargin_South	-120.398	36.202	-119.385	34.929	18	–	PC
Sargent_North	-121.926	37.120	-121.720	37.069	12	–	C
Sargent_South	-121.720	37.069	-121.471	36.919	10	2.9 ± 0.7	C
SargentClosure	-121.471	36.919	-121.449	36.933	0	–	C
MtLewisTrend	-121.678	37.684	-121.677	37.290	9	–	SC[c]
CalaverasSanAndreasPaicinesConnector	-121.407	36.843	-121.286	36.679	0	–	C
Paicines_North	-121.407	36.843	-121.064	36.523	9	6.0 ± 2.0	SPC
Paicines_South	-121.064	36.523	-121.042	36.448	0	–	SPC
ECSZ	-119.420	39.000	-116.249	33.804	15	–	SPC

from intentionally oversimplified (such as "TwoPlate") to those that are likely beyond the resolving power of our data ("Complex").

Fault Connections

Faults that are connected can transfer slip between one another and potentially rupture together in large earthquakes. Knowing if two faults connect, as well as the location and geometry of that connection, is therefore important in determining the seismic hazard associated with each fault [e.g., *Harris and Day*, 1999]. Such connections are often not mapped, or are mapped with such complexity that we must simplify their geometry. To define the block boundaries, we must make inferences about these connections. While these inferences add non-uniqueness to our models, this feature of block modeling also allows us to test various scenarios of fault connections to see if they are consistent with our observed surface deformation rates.

1.4.5 Surface Creep

A number of faults in the Bay Area exhibit surface creep and aseismic creep at depths shallower than the seismic/aseismic transition [see the comprehensive compilation of *Galehouse and Lienkaemper*, 2003]. Conclusions from detailed geodetic inverse modeling [*Manaker et al.*, 2003; *Schmidt et al.*, 2004], as well as comparisons between surface creep and geologic slip rates determined from paleoseismology show that the slip rate on the shallow portions of the fault during the interseismic period can be much slower than the deep slip rate [e.g., *Simpson et al.*, 2001]. Faults in the Bay Area that creep at the surface can slip as slow as 10% of the deep slip rate or as fast as the full deep slip rate [*Bakun*, 2003; *Prescott et al.*, 2003]. To simulate the effects of near-surface aseismic creep, we model shallow slip as a dislocation with uniform slip that runs from the surface to a certain "transition depth" (TD). The TD must be $\leq$ the fault locking depth (LD) because, by definition, the fault slips at a uniform rate below LD. The fault is locked at depths between TD and LD. Because the detailed distribution of creep at depth is not well known on all Bay Area faults, we assume the simplest case where TD=LD (the fault creeps at one uniform rate from the surface to LD, where it transitions to its deep slip rate at all depths below LD). We explore the depth sensitivity of TD in Section 1.6.6.

The shallow dislocation representing aseismic creep is completely independent from the block motion and is permitted to slip at any rate slower or faster than the deep slip rate if the data favor such behavior. We add a new term to Equation 1.1:

$$\mathbf{v}(\mathbf{r}_i) = \mathbf{\Omega}_i \times \mathbf{r}_i - \sum_{f=1}^{\#Faults} \left[\mathbf{G}_i^f \cdot \mathbf{s}^f(\mathbf{\Omega_i}) - \mathbf{G}_{creep,i}^f \cdot c^f \right] \tag{1.2}$$

where $\mathbf{G}_{creep,i}^f$ is the Green's function relating slip between the surface and the transition depth on fault f to deformation at station i. Unlike the deep slip rate, $\mathbf{s}$, that is a function

Table 1.3. Model name abbreviation key, listed in order of increasing complexity. The second section of the table shows abbreviations for variations on the 5 main models.

TwoPlate	Pure block offset between Pacific and North America. Excludes all GPS data in California and near plate boundaries. Included for comparison with previous global studies.
Simple	Includes the block offset, strain accumulation, and shallow creep on the major Bay Area faults as well as an ECSZ along the east edge of the Sierra Nevada range. Slip transfers from the Calaveras to the Greenville fault via the Mt. Lewis trend. The Calaveras connects to the Concord/Green Valley system eastward across a right step.
Preferred	Similar to the Simple model but slip on the Greenville fault connects to a fault running along the west edge of the Great Valley ("Valley Margin deformation zone"), and no Mt. Lewis trend is included. Calaveras connects to both the West Napa fault to the west and the Concord fault to the east. Preferred is our reference for comparison between the models and the basis for exploration of locking depths or geometric variations.
Complex	Includes all the faults in the Preferred model, along with more complex connections between the Calaveras and San Andreas faults, a Sargent fault, and a Mt. Lewis trend. This model is probably overly complex given our data resolution.
Calaveras West	Forces all slip on the northern Calaveras to transfer in a left-stepping sense onto the West Napa fault.
Calaveras East	Forces all slip on the northern Calaveras to transfer across a right step to the Concord fault.
LD= $D_{95} + 1$	Models where we explore locking depth variations. Locking depths start out equal to D_{95}, and then we shift them uniformly up or down by the given amount. Note: In our sign convention, +1 makes the locking depth deeper by 1 km, while -1 is closer to the surface.
LD=13	Sets the locking depth of all faults in the model equal to a uniform value (in this case, 13 km).
MtLewis=2	Imposes an *a priori* constraint on the slip rate of a single segment (in this case, the Mt. Lewis trend is set to $2 \pm 2mm \cdot yr^{-1}$).

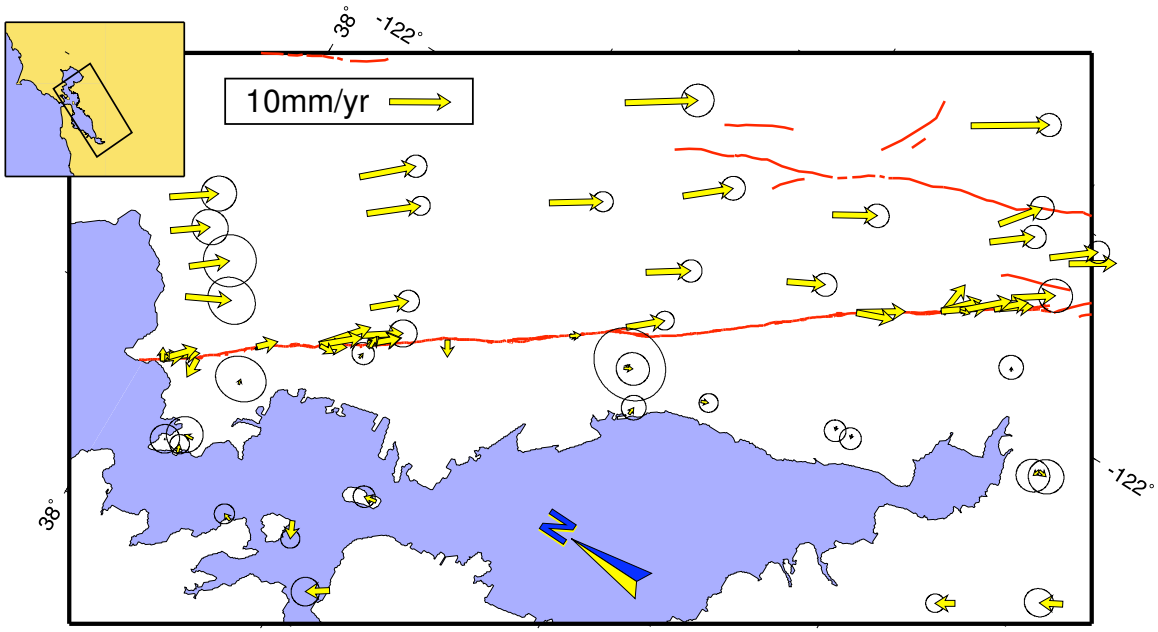

Figure 1.5. Map of deformation near the Hayward fault. See caption to Fig. 1.1. Here, stations adjacent to the Hayward fault are plotted without their error ellipses for clarity. The magnitude of the error ellipses are typically the size of the largest error ellipses on the map.

of the block rotation, $\mathbf{\Omega}$, the shallow creep rate, c, is a new model parameter that must be estimated. For segments where *Galehouse and Lienkaemper* [2003] observe a surface creep magnitude less than 1 $mm \cdot yr^{-1}$, we do not solve for a shallow dislocation and keep the fault completely locked above its locking depth. We only consider strike-slip motion on shallow dislocations, so c is a scalar.

BĀVŪ includes more than 60 stations within 15 km of the Hayward fault (Fig. 1.5), so we solve for 4 different shallow dislocations along strike. However, it is not possible to reliably constrain the surface creep rate for some Bay Area faults with GPS data alone because the stations are not typically located within a few kilometers of the fault. We therefore include the surface slip rates summarized in *Galehouse and Lienkaemper* [2003] as *a priori* constraints for the shallow slip rates with *a priori* uncertainties equal to the published uncertainties that include a random walk component. These uncertainties are sufficiently large such that the creep rate is determined largely by GPS data where stations are close enough to a fault to resolve shallow slip. Where data are absent, the *a priori* constraint stabilizes the inversion. Where segments span multiple observed surface creep rates that differ by values greater than their one-sigma confidence interval, we combine these values as weighted averages to determine a single constraint.

1.5 Results

We evaluated over 100 different variations on fault geometry to determine the models most consistent with the geodetic data and mapped faults. We report only a small subset of these models, highlighting the key parameters that affect model fit. Changes in model geometry (including fault connections, location, orientation, and locking depth) can affect the inferred fault slip rates greater than indicated by the formally propagated uncertainties from the inverse problem, which are typically $< 1.5\ mm \cdot yr^{-1}$ at the 95% confidence level. For the range of reasonable geometries we test, the slip rates on almost all faults are within $\pm 3\ mm \cdot yr^{-1}$ of the Preferred model, which we consider to be representative of the actual confidence interval of our slip rate estimates. For quantitative comparisons, we restrict our analyses to the formal uncertainties but note that this variation should be considered when interpreting our results.

To evaluate the effectiveness of the block model, we compare the input GPS velocities to model estimates calculated from the best-fitting parameters. Figure 1.3 and 1.6 show observed and modeled GPS velocities for our Preferred model at the scale of all California and the Bay Area, respectively. Overall, the model predictions agree quite well with the observations and we capture many of the details of deformation across the Bay Area. Examining the "residuals," or the difference between the data and model allows a more detailed comparison of the systematic differences between observations and predictions for several model variations (Fig. 1.7).

We quantify the goodness of fit in terms of the χ^2 and χ^2/DOF statistics:

$$\chi^2 = \sum_{c=1}^{\#data} \left(\frac{v_c^{model} - v_c^{data}}{\sigma_c} \right)^2 \tag{1.3}$$

$$\chi^2/DOF = \frac{\chi^2}{\#data - \#model\ parameters} \tag{1.4}$$

where v_c^{model} and v_c^{data} are the predicted observed velocity components, and σ_c is the 1σ uncertainty for each component of the input GPS velocities. The number of degrees of freedom (DOF) is defined by: $\#data$, the number of GPS components used as input data (east and north component for each station, as well as any *a priori* constraints) and $\#modelparameters$, the number of model parameters that we solve for in the inversion (pole of rotation latitude and longitude, rotation rate, and shallow creep rate for creeping segments). These statistics indicate how well the model fit the data within their uncertainty bounds. Lower values of χ^2 indicate a better fit to the data. χ^2 can be calculated for a single data component or summed over subsets of the model, including both horizontal components at a single station or the entire model. Increasing the number of model parameters inevitably leads to better fits and lower total χ^2. Dividing by the number of degrees of freedom (DOF) helps us compare models where we solve for a different number of free parameters, but χ^2/DOF ignores all correlations between parameters. Because these correlations change as model geometry changes, caution should be exercised in making strictly quantitative comparisons of models using χ^2/DOF alone. Nonetheless, the statistics do provide a basis

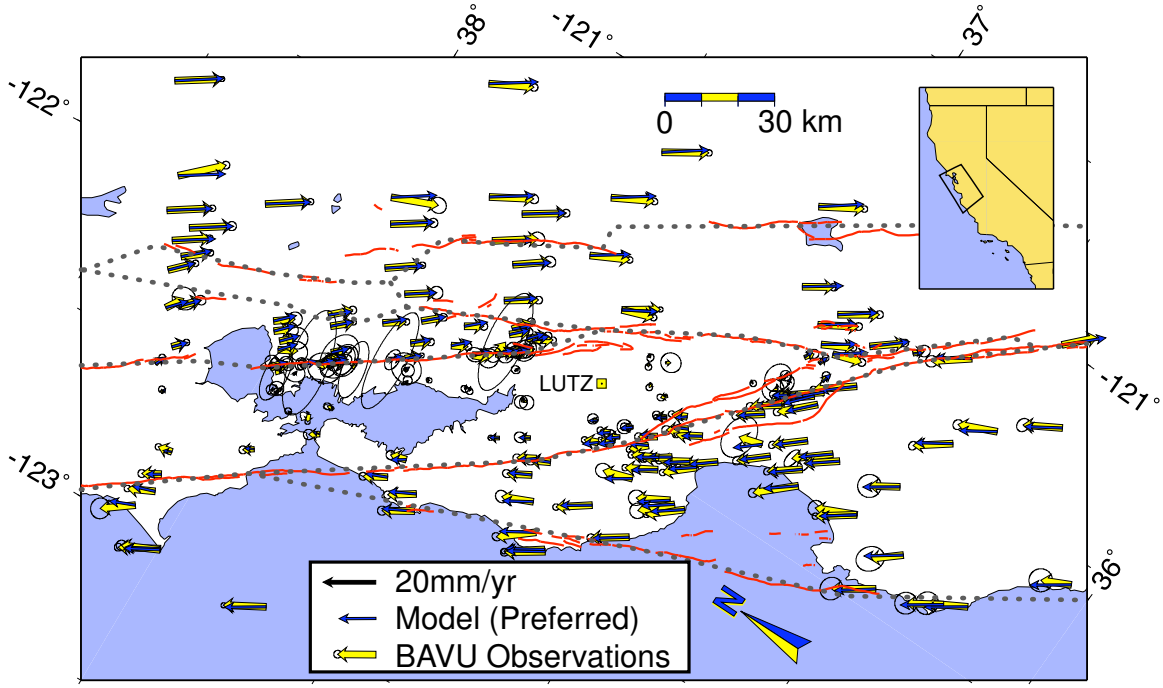

Figure 1.6. Observations (wider vectors with error ellipses) compared with model results (narrow, darker vectors) for our Preferred model. Dotted grey lines on top of mapped fault traces are model geometry.

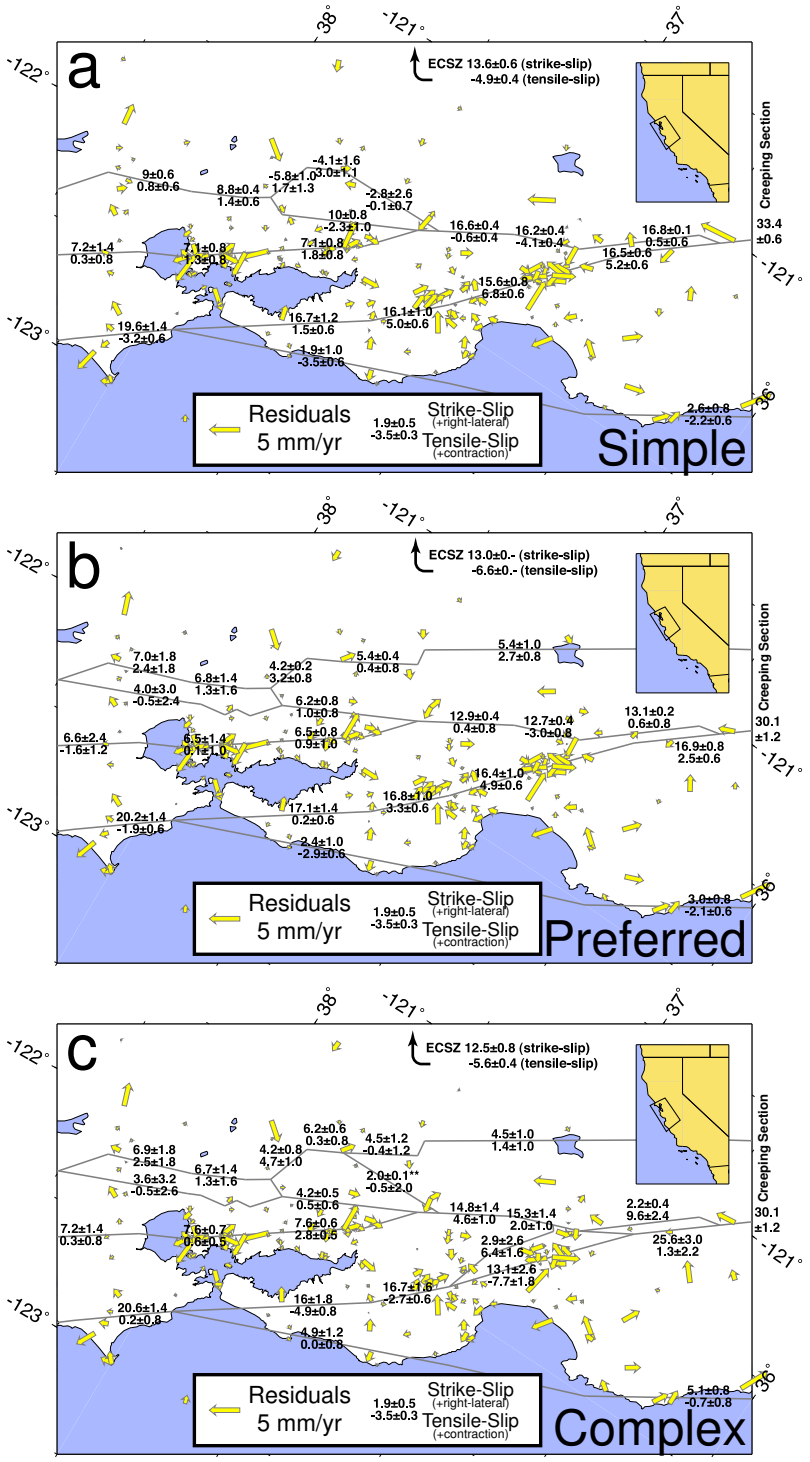

Figure 1.7. Difference between observed GPS velocities and model calculations for three different model scenarios. Numbers indicate strike-slip and tensile-slip rates and 95% (2σ) uncertainties for select fault segments. Positive strike-slip indicates right-lateral slip. Positive tensile-slip indicates contraction while negative tensile-slip indicates extension.

Table 1.4. Misfit statistics for different models. Note that TwoPlate excludes all data within 100 km of the plate boundary.

Model	χ^2	**DOF**	χ^2**/DOF**
TWOPLATE	138.9	45	3.09
SIMPLE	2053.8	520	3.95
PREFERRED	1880.0	517	3.64
COMPLEX	1704.8	510	3.34
Variations on models			
CalaverasWest	1932.5	520	3.72
CalaverasEast	1910.7	520	3.67
Preferred, Thrust	1887.9	517	3.65
Preferred, Unclamped	1871.1	514	3.64
Preferred, LD=$D_{95} - 8$	1911.9	517	3.70
Preferred, LD=$D_{95} - 5$	1795.5	517	3.47
Preferred, LD=$D_{95} + 5$	2053.9	517	3.97
Preferred, LD=5	1923.0	517	3.72
Preferred, LD=8	1805.9	517	3.49
Preferred, LD=13	1875.0	517	3.63
Preferred, LD=18	2047.1	517	3.96
Preferred, TD=5	1997.9	517	3.86
Preferred, TD=$D_{95}/2$	1986.5	517	3.84
Preferred, WG03	3675.7	539	6.82

for qualitative comparisons. For uncorrelated parameters, a χ^2/DOF of 1 indicates that, on average, all the predicted velocities are consistent with the 1σ standard deviation of the input data. In Table 1.4, we present misfit statistics for the models we discuss. We typically obtain χ^2/DOF of 3-4, which is partly the result of the χ^2 statistic's strong sensitivity to outliers. Because of these outliers, we emphasize the spatial distribution of the contribution to χ^2 when comparing models.

In the following sections, we look in detail at the model results at a range of scales from global motions to the details of fault connections and stepovers.

1.5.1 Global Plate Motion

To verify that our block model provides valid constraints on the total relative plate motion, we compare them with previously published results in Table 1.5. Our estimates of relative rotation axes incorporate the effect of elastic strain accumulation while the previous studies of block motion typically exclude data from near plate boundaries. With the exception of NUVEL-1A and *DeMets and Dixon* [1999], each study shown is based on geodetic measurements using VLBI and/or GPS. In general, the geodetic measurements show a relative pole of rotation between the Pacific and North American plates that is further to the

northeast and faster than the average rate for the last 3 Ma determined from geologic data [NUVEL-1A, *DeMets et al.*, 1994]. Variations in the estimated rotation axes from each study stem not only from the different quality data sets available to each author at the time of publication, but also the stations they use to define each rigid plate. To verify the quality of the BĀVŪ global velocities, we use our block modeling code and the identical subset of stations from *Steblov et al.* [2003]. Our results agree almost identically to their published results, though our propagated uncertainties are slightly smaller. In our model called "TwoPlate," we include all 21 North American and 6 Pacific sites from BĀVŪ that are further than 100 km from a plate boundary. The pole of rotation from TwoPlate is 1.7° east, 1.3° north, and 0.5% slower than the *Steblov et al.* [2003] pole, but the change is not significant at the 95% confidence level. The estimated pole from our "Preferred" model is about 0.9° east, 1.1° north, and 0.9% slower than the *Steblov et al.* [2003] pole. Globally, our data set and block modeling produce reasonable estimates of block motion.

Locally, the slight changes in the NA-PA rotation axis are insignificant. Table 1.6 shows the rate at the Farallon Islands station, FARB, predicted from the NA-PA rotation axis. The station is located on the Pacific plate about 36 km west of of the San Andreas fault and its velocity is sometimes used as a proxy for the total relative motion between the Pacific and North American or SNGV plates [e.g., Table 4 of *Prescott et al.*, 2001]. The long term rate of block offset is higher than the current observed velocity at FARB. Strain accumulation along Bay Area faults "slows down" FARB by about 3 $mm \cdot yr^{-1}$. As such, the observed rate of FARB is not representative of pure Pacific plate motion and should not be directly compared with studies that ignore elastic strain accummulation.

1.5.2 Sierra Nevada / Great Valley Block

Focusing in on California, the Sierra Nevada/Great Valley (SNGV) block is a rigid block that lies at the eastern margin of the Bay Area. Often referred to as a microplate, the relative motion of the SNGV is not as well constrained as larger plates because of the limited size of the block and relatively sparse data. By including stations from throughout northern and southern California along with strain accumulation near the block boundaries, our block model provides an improved constraint on the total PA-SNGV motion that must be accommodated by Bay Area faults. Table 1.5 shows our estimates of the relative motion between PA-SNGV and NA-SNGV compared with previous studies.

In general, the NA-SNGV pole tends to lie southwest of the Bay Area in the Pacific Ocean, as far as 90° from the NA-PA pole. The relative motion expected from these two poles differs in a manner consistent with geologic observations: the relative motion vector from NA-PA in the Bay Area is oriented within a few degrees of the strike of the San Andreas system promoting nearly pure transform faulting, while the NA-SNGV motion would require a substantial amount of opening along such faults relative to the strike-slip component – a feature that manifests itself as extension on the ECSZ and in the Basin and Range further to the east. The NA-SNGV poles from previous studies vary by $> 50°$ in both longitude and latitude, and our results show a similarly broad range due to slight variations in fault geometry and locking depth. These estimates seem to lie along a great

circle roughly perpendicular to the average fault strike in the San Andreas fault system and are related to station geometry. The ideal station coverage for determining rotation axes covers a very broad area in all directions. The SNGV and other Bay Area blocks are elongate parallel to the San Andreas system and very narrow perpendicular to it. The orientation of elongated error ellipses for these poles is related to the elongated shape of the blocks.

The PA-SNGV pole is well constrained and located just west of Lake Superior, $\sim 20°$ from the NA-PA pole. Unlike NA-SNGV, formal uncertainties for this pole location are $< 3\circ$, and the best-fit estimates vary by only $\pm 6°$ for a wide range of model geometries. The pole for PA-SNGV is more tightly constrained and is much less affected by the tradeoff between pole position and rotation rate than the NA-SNGV pole.

1.5.3 Poles of Rotation of Bay Area Blocks

Focusing in on the Bay Area itself, we can examine rotation axes of smaller blocks bounded by Bay Area faults. Figure 1.8 shows the pole of rotation of each block relative to North America. There is a systematic progression of the poles from west to east. In our Preferred model, the poles essentially transition between the NA-SNGV and NA-PA poles. The Santa Cruz block, located adjacent to the Pacific plate, rotates about a pole located near the NA-PA pole. On the other side of the Bay Area, the Coalinga block, located adjacent to the SNGV block, rotates about a pole located very close to the NA-SNGV pole. These blocks near the margins of the Bay Area move very similarly to the larger blocks that bound the region. Blocks within the Bay Area have rotation poles relative to North America in between these poles, with blocks toward the eastern side of the Bay Area tending to move more like NA-SNGV and blocks on the western side moving more like NA-PA. This pattern holds for variations in locking depth and slight variations in geometry on the Preferred model. For the Complex model, the poles of Bay Area blocks are still distributed between the NA-PA and NA-SNGV poles, but the east-west progression breaks down slightly as many of the smaller blocks rotate about poles very close to the blocks themselves. These rotations would result in gradients in slip rate along strike. With the station geometry of BĀVŪ, there is a strong trade-off between the rotation rate and distance of the poles of rotation from the Bay Area.

The limited extent of the blocks allows these different rotation axes to produce nearly identical relative motions in the Bay Area, resulting in the elongated error ellipses for these poles.

1.5.4 Slip Rates on Bay Area Faults

One of the most useful products that geodesy provides to seismic hazard estimates is constraints on the deep slip rates of faults. As described in Section 1.4.2, our block model uses GPS observations of surface deformation to calculate the best fitting deep slip rate from given block/fault geometries and locking depths. Here we present a general discussion

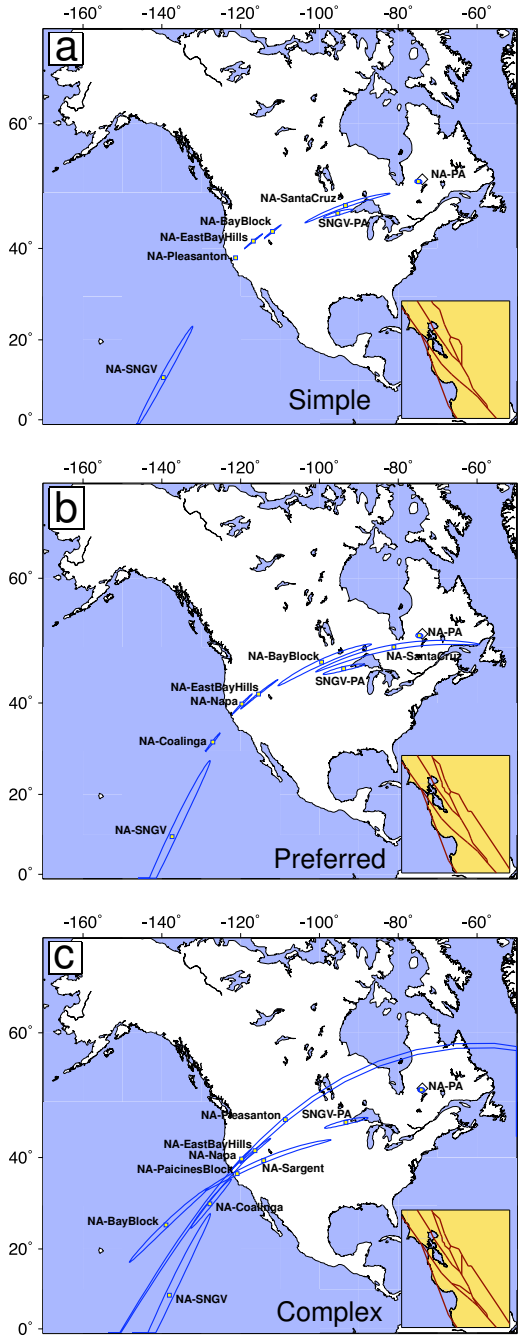

Figure 1.8. Calculated poles of rotation and 95% confidence limits for blocks in the Bay Area. Other than the Pacific-SNGV pole, all poles are relative to North America (NA). The diamond near Hudson Bay indicates the PA-NA pole for TwoPlate, which excludes data near plate boundaries.

about the effect of variations in locking depth on estimated slip rates (also see Section 1.6.6), and we present slip rates using our preferred locking depths.

Locking Depth

Freymueller et al. [1999] described the strong trade-off between assumed locking depth and calculated slip rate in dislocation models of the San Andreas system in northern California, making it challenging to uniquely determine the slip rate on a given fault. As a result, several methods including bootstrap resampling [*Murray et al.*, 2001] and Bayesian statistics [*Segall*, 2002] have been used to place statistical bounds on the range of most-likely slip rates given this tradeoff. Without additional physical constraints, such methods remain purely statistical descriptions of the uncertainty and do not help resolve the non-uniqueness problem. *Segall* [2002] advocates integrating prior information about the slip rates from geologic studies and earthquake parameters. Because one of our goals is to estimate these rates geodetically, we take an alternate approach.

The maximum depth of seismicity and surface heat flow give insight into the depth of the seismic/aseismic transition. Using this depth as a proxy for the geodetic locking depth helps reduce the ambiguity in determining slip rates. Earthquakes rarely occur below 20 km depth in the Bay Area, and the specific depth where faults become seismically quiet varies spatially throughout the region. Many geodetic studies use seismicity to define the locking depth in their models, but they sometimes neglect variations within the fault system. Here we document temporal and spatial variation in the depth of seismicity throughout the Bay Area in order to accurately determine the seismic-aseismic transition depths.

This transition is commonly quantified by the depth at which 95% of catalog seismicity occurs above and 5% occurs below, or D_{95}. *Williams* [2003] suggests that D_{95} accurately reflects the deepest extent of rupture in large earthquakes and presents the calculated values of D_{95} for Bay Area fault segments derived from high quality Northern California Seismic Network (NCSN) catalog locations from 1980-1998. We perform a similar analysis on the high precision catalog of *Waldhauser and Ellsworth* [2002]. This catalog utilizes relative relocations that have vertical precision of less than about a hundred meters. We divide the Bay Area into a data-driven grid using the quadtree algorithm with a minimum grid cell size of 0.2 degrees [*Townend and Zoback*, 2001]. Figure 1.9 shows the depth of maximum seismicity for the entire duration of the catalog (1984-2001) and a movie in the electronic supplement shows the time evolution of D_{95}. In both illustrations, grid cells are only filled with a color if there are more than 60 events during the time period indicated in the lower left. This number of events seems to produce consistent and stable values for D_{95} [*Magistrale*, 2002].

We do not utilize the D_{95} value as the locking depth for two fault segments. The Marin segment of the San Andreas fault has essentially no seismicity, so we cannot calculate D_{95}. The grid cell south and the grid cell west of it both have locking depths close to 12 km. However, using a locking depth of 15 km provides a better fit to the geodetic data.

D_{95} on the Greenville fault is very deep in the north near Mt. Diablo (18 km), but gets

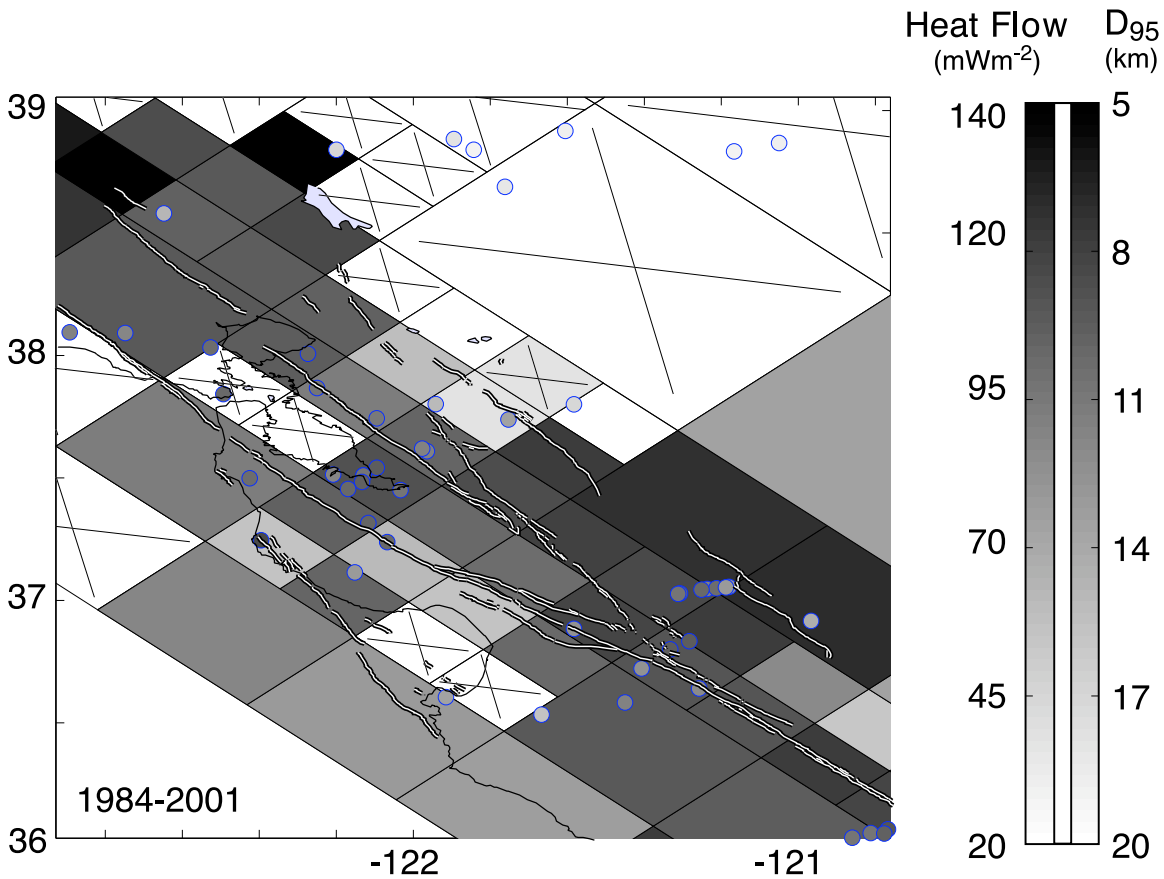

Figure 1.9. D_{95}, the depth at which 95% of the seismicity in a certain area is above and 5% is below, indicated by shading of rectangular grid cells. Earthquakes from 1984-2001 using the relative relocation catalog of *Waldhauser and Ellsworth* [2002]. Shaded circles are borehole heat flow measurements from the USGS California Heat Flow database [http://quake.wr.usgs.gov/heatflow/]. The two data sets are plotted using similar color schemes so that shallow D_{95} depths and high heat flows both appear in the same color. While the data sets are often well correlated, the relationship depends on rock type and may not be linear as implied by the shared color scheme [see *Magistrale*, 2002]. D_{95} not estimated for grid cells with < 60 events (cells with X's).

much shallower in grid cells to the south (other than the Geysers, these 3 grid cells have the shallowest seismicity in the Bay Area with values of 8-9 km). A much better fit is achieved to the data if the 18 km locking depth is extended further south along all of the segments, including the fault along the margin of the Great Valley. Heat flow data are sparse in this region, but available data near the Ortigalita fault range from $65 - 85 mWm^2$ [*Lachenbruch and Sass*, 1980], values more consistent with a locking depth of 8-12 km, based on the relationships established by *Williams* [1996]. The model preference for a deeper locking depth results in deformation over a broader region surrounding the single block boundary in our model, which could be indicative of a broader deformation zone in this region.

Slip Rates

Deep slip rates determined by our block model are reported in Table 1.7. The total vector sum of relative motion accommodated by Bay Area faults in the Preferred model is $37.9 \pm 0.6\ mm \cdot yr^{-1}$ oriented at $N30.4°W \pm 0.8°$ in the central North Bay and at $N34.2°W \pm 0.8°$ in the central South Bay (Rate varies by 1-2 $mm \cdot yr^{-1}$ from east to west across the Bay Area, while azimuth varies by up to 8° from north to south).The simple sum of all strike-slip rates across the entire fault system for our Preferred model is 37.8 ± 4.5 and $37.7 \pm 1.5\ mm \cdot yr^{-1}$ in the northern and southern Bay Area, respectively. We report slip rate uncertainties at the 95% confidence level (2σ). The total best-fit slip rate ranges from 31.5-39.3 $mm \cdot yr^{-1}$ for the different fault geometries and locking depths we have explored. The Simple model consistently produces the lowest total slip rate. Within the Preferred model, the total slip is a strong function of assumed locking depth. The total best-fit slip rate ranges from 34.6-39.3 $mm \cdot yr^{-1}$ as we vary the locking depth over a range of 13 km. Some models show a total slip rate 1-2 $mm \cdot yr^{-1}$ faster in the northern Bay Area than a profile taken in the south, but this difference is smallest in the Preferred model. These values are slightly lower than the total PA-SNGV motion in the Bay Area because some of the motion in the model is accommodated by tensile-slip on the faults.

We highlight the slip rates of a few key fault segments. Our model provides a robust estimate of slip on the San Gregorio fault. Because this fault is partly offshore in the Bay Area it is very difficult to estimate a rate using independent dislocations and onshore data. Our block model includes global stations to help constrain the motion of the Pacific block relative to the Bay Area. The resulting slip rate on the San Gregorio fault from our Preferred model is $2.4 \pm 0.5\ mm \cdot yr^{-1}$ near the Golden Gate, with a slightly higher rate off of Monterey Bay.

We include the West Napa fault in some models, as it may be the northern continuation of the Calaveras fault along a series of westward steps [J. Unruh, pers. comm., 2004]. We find that its slip rate ranges from 3.4 - 7.4 $mm \cdot yr^{-1}$ across all models, with most models estimating slip rates near the lower end of this range. Models where 100% of the slip on the northern Calaveras fault transfers to the West Napa fault produce the higher slip rates. In our Preferred model it slips at $4.0 \pm 3.0\ mm \cdot yr^{-1}$. This is the highest formal uncertainty for any deep slip rate in the inversion. In models where the West Napa fault and the Green

Valley fault are both allowed to carry some of the Calaveras slip, the slip rates of the two faults sum to 9.5-11.0 $mm \cdot yr^{-1}$, depending on model geometry and locking depth.

Models where we include a fault along the western margin of the Great Valley produce systematically better fits to the data than those that exclude this fault. This fault follows the eastern front of the Coast Range, passing along the Ortigalita fault. We find a strike-slip rate of 5.4 ± 1.0 $mm \cdot yr^{-1}$ in our Preferred model, and the rate typically varies between 4-6 $mm \cdot yr^{-1}$.

1.5.5 Shallow Creep

Table 1.9 shows the best-fit slip rates along dislocations that intersect the surface (surface creep) in our Preferred model. These rates typically vary by < 0.5 $mm \cdot yr^{-1}$ between most model geometries. Because data coverage is sparse in some areas, the formal uncertainties in creep rates are larger than for the deep slip rates. The uncertainties are smallest on the Hayward fault (1.2-1.4 $mm \cdot yr^{-1}$) and largest on the southern Calaveras (> 6 $mm \cdot yr^{-1}$).

Figure 1.10 shows a comparison of the best-fit slip rates from the model with observations along the Hayward fault where we have the most near-fault data. While influenced by the *a priori* creep rate constraints which are based on the *Lienkaemper et al.* [2001] data set, the results differ by < 1 $mm \cdot yr^{-1}$ when no constraints are applied and the data are allowed to control the shallow slip rate completely.

In all cases except two, the best-fitting shallow slip rate is less than the best-fitting deep slip rate. Forcing the creep rate on the southern Calaveras fault to be equal to the deep slip rate increases the χ^2/DOF by an insignificant 0.4%, as there is little data coverage in this region. For the San Andreas fault south of San Juan Bautista (Segment SanAndreas-SJB), the calculated shallow slip rate of ~ 20.3 $mm \cdot yr^{-1}$ exceeds the deep strike-slip rate of ~ 16.4 $mm \cdot yr^{-1}$. The higher slip rate is favored in models without *a priori* constraints and produces a 4% reduction in misfit compared to a model where the shallow and deep segments are required to slip at the same rate. While surface creep rates near San Juan Bautista accelerated following the 1989 Loma Prieta earthquake to rates > 20 $mm \cdot yr^{-1}$ [*Behr et al.*, 1997], creepmeter data during the timespan of the BĀVŪ data show a surface creep rate of 12-13 $mm \cdot yr^{-1}$ from 1993-2003 (instruments XSJ2, XHR2; data from http://quake.wr.usgs.gov/research/deformation/monitoring/data.html).

Even though no surface creep is observed north of Nyland Ranch [about 1.4 km north of San Juan Bautista, *Galehouse and Lienkaemper*, 2003], we find that the GPS data favor extending shallow creep about 15 km north of San Juan Bautista with a constant rate of 9.0 ± 2.0 $mm \cdot yr^{-1}$. This rate is lower than sections further south, consistent with a relatively smooth transition between creeping and locked behavior. While allowing shallow slip to extend 15 km north of San Juan Bautista (as we do in our Preferred model) reduces the total misfit, there are still very high residuals in this region in all model variations. *Johanson and Bürgmann* [2004] show that slip in this area is spatially complex.

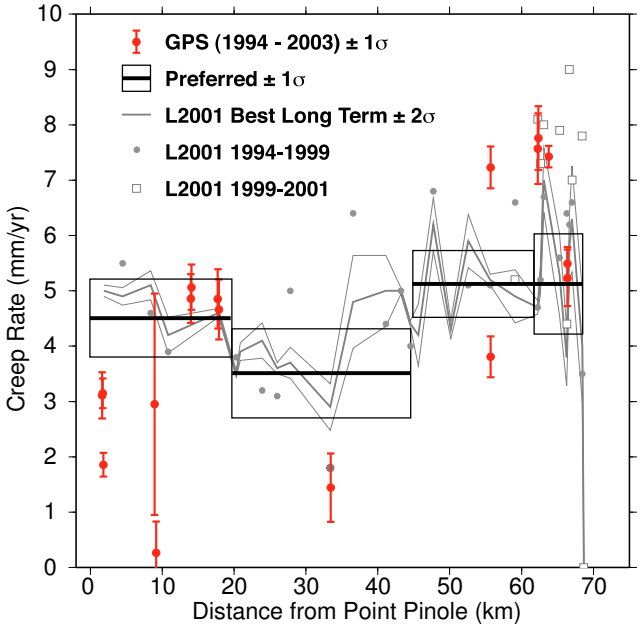

Figure 1.10. Comparison between best-fit shallow slip rate from model and observations of surface creep rate, shown as a function of distance along strike of the Hayward fault. Model results and propagated uncertainties for four shallow dislocations are shown as the horizontal lines with boxes. GPS observations (circles with error bars) are calculated from BĀVŪ. Triangulation data from different time periods (dots, open squares) as well as the best long term average (medium line) and associated error bounds (thin lines) from *Lienkaemper et al.* [2001]. GPS surveys occupy the same survey benchmarks as the triangulation surveys, but span different times. Each GPS observation spans a slightly different time span within the range of 1994-2003.

1.6 Discussion

1.6.1 Comparing the Models

Figure 1.11 shows the residuals for the three main model geometries we discuss. The shading in Figure 1.11a show the spatial distribution of the contribution to the total χ^2 misfit. Larger values (darker colors) indicate that the model is doing a particularly poor job of fitting the data in a certain area. The fit in the central Bay Area is overall quite good. There are a few stations that show up as strong outliers, such as the station in the upper-left corner of the map (CAML). The area around the epicenter of the 1989 Loma Prieta earthquake in the Santa Cruz Mountains has a consistent pattern in the residual velocities and a high total misfit. The orientation of the residuals is most systematic northeast of the fault where the data could be fit by a higher right-lateral slip rate and $< 1\ mm \cdot yr^{-1}$ of fault perpendicular motion on this section of the San Andreas fault. Such an observation might indicate that accelerated postseismic deformation along the fault persists at rates of $\sim 1\ mm \cdot yr^{-1}$ more than a decade after the 1989 earthquake. The block model cannot fit a localized area of accelerated deep slip because it must make slip along the entire San Andreas compatible with one block rotation. Stations nera San Juan Bautista, also along the San Andreas fault, are fit poorly, though the orientations of residual velocities are not entirely systematic. Together, the two areas along the San Andreas fault in the southern Bay Area and a few strong outliers dominate the χ^2 statistics. Models that improve the fit of those regions may have lower total χ^2 even if they result in a worse fit throughout the rest of the model.

The shading in Figs. 1.11b-c and 1.12 show where the weighted residuals (χ^2) for each model differ from the Preferred model. We calculate χ^2 for the two components of each GPS velocity in each model and then subtract this from χ^2 in the preferred model. Note how changes to the geometry of the model in one location can alter the predicted velocity throughout the model.

The Simple model (Fig. 1.11b) fits Bay Area GPS data within the uncertainty about as well as the Preferred model. However, the model does a poor job fitting sites east of the Calaveras and San Andreas faults in the southern Bay Area. Figure 1.3b shows that the fit to sites on the SNGV block is also poorer in the Simple model, with a systematic rotation of the predicted velocities to the east (clockwise) of the data. The slip rate on the Mt. Lewis Trend and Greenville faults is left lateral for the Simple model, which is the opposite sense to the required interpretation from earthquake focal mechanisms in the region [e.g., *Kilb and Rubin*, 2002]. The systematic misfit of GPS data in northern California and the opposite sense of slip are the motivation for including a "Valley Margin deformation zone" in our Preferred model. *Unruh and Sawyer* [1998] suggest that the Greenville fault connects with the Ortigalita fault, a Holocene-active fault with both vertical and strike-slip components that parallels the San Andreas fault system along the eastern margin of the Coast Range [*Bryant and Cluett*, 2000]. We extend a vertical fault through the trace of the Ortigalita fault, connecting to the San Andreas at the Carrizo Plain in the south and to the Greenville fault in the north. Geologic and geophysical evidence supports the existence a major fault structure in this vicinity along the eastern front of the Coast Range [e.g., *Wong and Ely*,

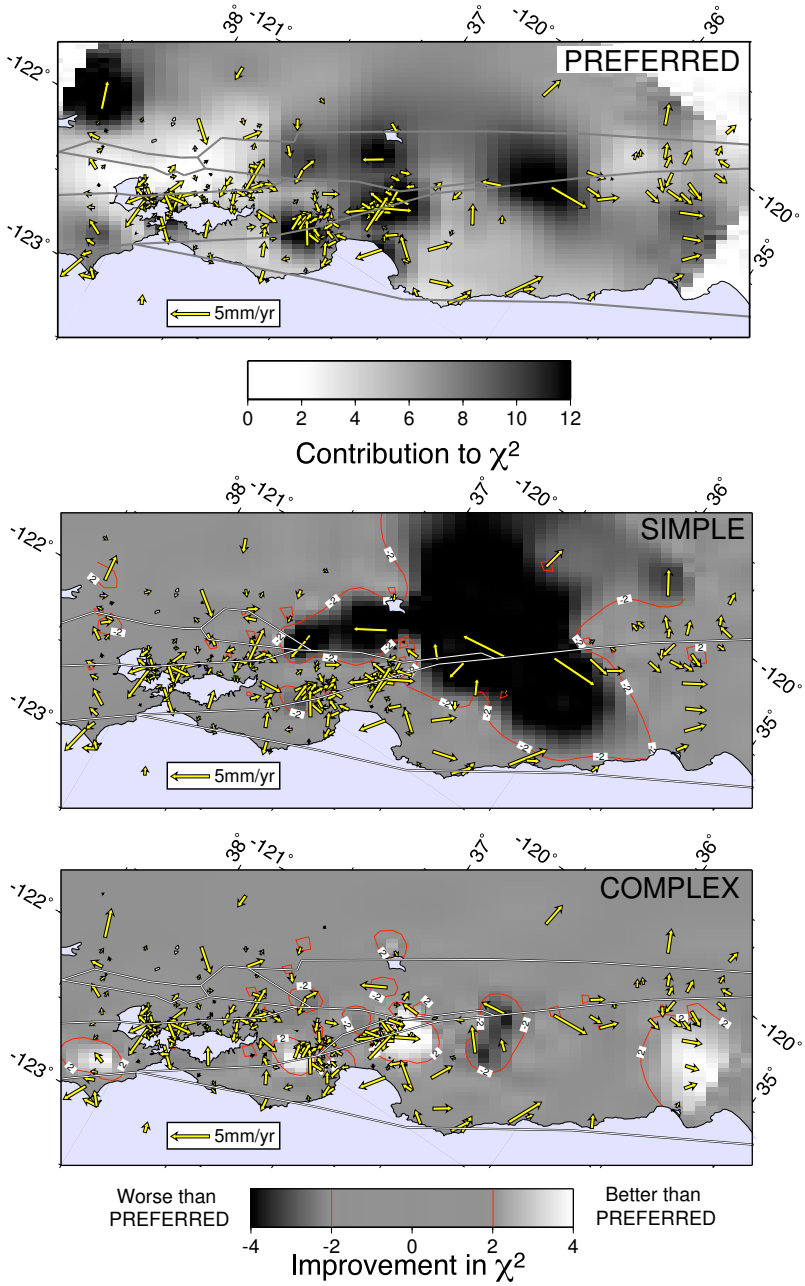

Figure 1.11. Residual velocity (difference between data and model) for three different model geometries. Shading in top panel shows relative contribution to the χ^2 misfit statistic of each station in our Preferred model. Dark colors indicate that the model does a poor job of fitting the data within its error bounds. Bottom two panels use a color scale that highlights differences between the given model and the Preferred model. Values of $|\chi^2| \leq 1$ for each data parameter indicate that the residual velocity is the same magnitude as the 1σ uncertainty. Contour lines at ± 2.

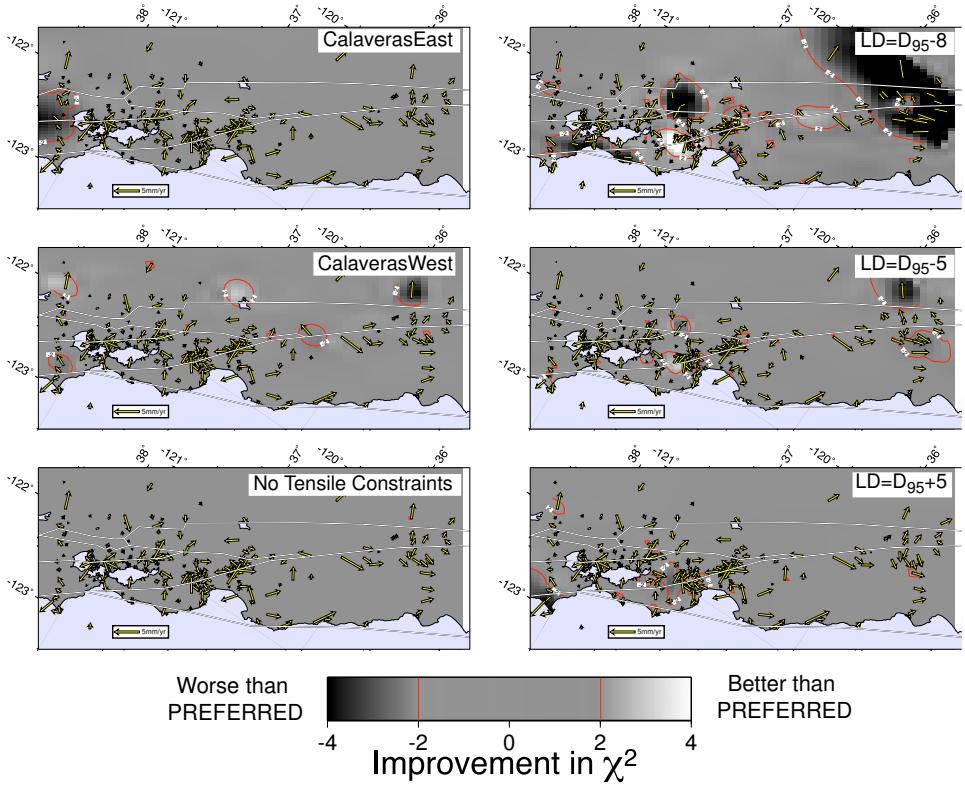

Figure 1.12. Residual velocity (difference between data and model) for multiple model variations. See caption to Fig. 1.11 for explanation.

1983; *Wentworth and Zoback*, 1989, 1990; *Fuis and Mooney*, 1990]. However, that specific structure may not be the active feature bounding the Bay Area and the Great Valley today. Seismicity, including the 1983 Coalinga event [*Wong and Ely*, 1983] suggest that a broad zone of faults may actually be accommodating the total relative motion across the Coast Range, and not a single discrete structure. Because the GPS data are sparse in this region, we are not able to differentiate between a single fault structure and a zone of faults along the eastern Coast Range, nor are we sensitive to the dip of the structure or structures. If deformation at this boundary is distributed over a broad zone, the measured slip rate along any individual structure in the field (such as the Ortigalita fault) would be smaller than the aggregate rate across the whole range calculated in our models for the Valley Margin deformation zone fault.

The Complex model (Fig. 1.11c) provides strong improvement to the model fit in some areas, particularly the areas most poorly fit in the preferred model near Loma Prieta and San Juan Bautista. These improvements are substantial and result in an 8% reduction in total χ^2/DOF even though there are some areas where the fit is slightly poorer in the Complex model than the Preferred model. The Complex model has three blocks (Pleasanton, Sargent, and Paicines) added to the Preferred model's 8 blocks. The Paicines block only has a single GPS station on it and is therefore poorly constrained by the data. Improved fit to data around San Juan Bautista accounts for the greatest reduction in misfit – probably because we add two additional blocks (Sargent and Paicines) in this area. The inferred slip rates in this region might not represent the unique motion of independent blocks, but rather the exploitation of additional degrees of freedom in the model. Unlike southern California, there is minimal geologic evidence for blocks rotating about poles within the boundaries of the blocks themselves [e.g., *Jackson*, 2002]. Even though this model has the lowest misfit, the sparse data coverage on these blocks and the known complexity of slip in this area suggest that the Complex model may not be the most accurate block model representation of the fault system in the southern Bay Area.

1.6.2 Dipping faults

All fault segments in our model are vertical, and in this section we discuss the technical and conceptual limitations to using dipping faults in a block model based on dislocation theory. We describe the challenge of determining how faults connect from mapped fault traces that do not intersect in Section 1.4.4. This problem is amplified in 3-D, as we define a network of interconnecting faults along the 3-D boundaries of the block. Besides the structural geology problem of defining fault geometry, the mathematical implementation of dipping faults for dislocation models is better suited to environments where thrust geometry is well determined and the fault dip is relatively constant. In the "backslip" implementation of our block model, we assume that faults have a constant dip along their entire extent. For faults like the Las Trampas blind thrust that dips towards the Hayward fault, the two faults should intersect at depth in the real world [see *Unruh et al.*, 2002]. The numerical implementation of our model, however, effectively treats the system as two dislocations extending to infinite depth. While there are alternate physical interpretations of the mathematical formulation of our model that involve a the elastic limit of a viscoelastic lower crust [*Meade*

and Hager, 2004], there are limitations when using of models based on deep dislocations in complex structural environments.

For vertical faults throughout all our models, we allow for the faults to open or the blocks to converge as a proxy for dip-slip faulting. This "tensile-slip" component (Table 1.8) accurately represents the total block motion, but the symmetric strain accumulation about a vertical fault is not a perfect analog for dipping faults. The differences between dip-slip and tensile-slip are pronouced for vertical deformation, but the differences are minor when only modeling horizontal components of GPS velocity.

Because thrust faulting may be important locally in the eastern Bay Area, we explore a variation on the Preferred model that includes dipping Mount Diablo and Mount Oso thrust faults ("Preferred, Thrust"). For the area where the structural environment is most complex to the northwest of the Calaveras fault, we use only vertical faults even though there is geologic evidence for dipping blind thrust faults [*Unruh et al.*, 2002]. Using dipping faults for these segments causes a substantial increase in χ^2 and reduces the slip rate on the Hayward fault by $\sim 1.5\ mm \cdot yr^{-1}$. The effect on the Hayward occurs because the bottom edge of the locked thrust faults is virtually collocated with the bottom edge of the creeping Hayward fault. The inversion is therefore not able to reliably distinguish between slip on the two faults. The χ^2/DOF for "Preferred, Thrust" is just 0.2% higher than the Preferred model and all slip rates are within $0.2\ mm \cdot yr^{-1}$ of the Preferred model.

With our block model, we provide geodetic constraints of active thrust faulting on the Mount Diablo fault system. All of our model geometries produce convergence across the Mount Diablo fault. Variations on the Simple and Complex models that include a dipping Mount Diablo fault find it has a reverse-slip of 2.7 and $5.7\ mm \cdot yr^{-1}$, respectively. In the "Preferred, Thrust" model, we find $3.9 \pm 0.5\ mm \cdot yr^{-1}$ of reverse-slip along with $4.2 \pm 0.5\ mm \cdot yr^{-1}$ of strike-slip across the fault. The reverse component is within the 1.3-7.0 $mm \cdot yr^{-1}$ range determined from restorations of geologic cross sections [*Unruh and Sawyer*, 1997]. The ratio between strike-slip and horizontal shortening components depends entirely on fault strike, but the total magnitude of the slip vector does not. The dip-slip magnitude is particularly sensitive to fault dip because horizontal shortening is projected onto the dipping fault. We use a dip of $38°N$ for the Mount Diablo thrust, based on the $30 - 45°$ range in *Working Group on Northern California Earthquake Probabilities* [2003]. Because of the Mount Diablo thrust system's role of transferring slip from the Greenville fault to the Concord/Green Valley system in our model, it must carry several $mm \cdot yr^{-1}$ of slip consistent with block motion. In addition to any shortening, a substantial portion of this slip must be strike-slip deformation because the thrust system's average strike is not perfectly perpendicular to the relative block motion that it must accommodate.

1.6.3 Convergence in the Coast Range

Perfect transform faulting can occur when the rotation axes for a sequence of blocks are located at the same point but have different rates. Faulting will only be pure strike-slip if all of the block boundaries are parallel to the small circle path of the relative motion vector and parallel to one another. The situation in the Bay Area meets neither of these conditions

perfectly – the rotation axes of Bay Area blocks follow a systematic progression between the NA-PA and NA-SNGV blocks, and the faults in the system are rarely parallel to one another. The Bay Area system could therefore allow a certain amount of fault-perpendicular motion. Abundant folds and thrust faults roughly parallel to the San Andreas system suggest that pure strike-slip motion on the major Bay Area faults does not accommodate all of the plate boundary motion. We use our block model to constrain the magnitude and location of any fault-perpendicular convergence.

Savage et al. [1998] use trilateration measurements collected over nearly 20 years to determine the regional strain field in the Bay Area. They find that the Bay Area as a whole undergoes an insignificant amount of areal dilatation. They identify localized zones where contraction would give rise to thrust faulting such as the region around the 1989 Loma Prieta rupture.

In contrast to the trilateration work, some authors suggest that Bay Area GPS data require a small component of fault-normal contraction between the SNGV block and the Bay Area. *Prescott et al.* [2001] analyze a profile between Point Reyes and Davis and find $\sim 3.8 \pm 1.5\ mm \cdot yr^{-1}$ of shortening over a 25-km-wide zone localized at the margin of the Great Valley. For a similar time span and data covering a larger range of latitudes in the Bay Area, *Murray and Segall* [2001] find $\sim 2.4 \pm 0.4\ mm \cdot yr^{-1}$ of contraction accommodated over a similarly narrow (<15km) zone. *Freymueller et al.* [1999] present data from further north and conclude that shortening must be less than $1 - 3\ mm \cdot yr^{-1}$. *Pollitz and Nyst* [2004] fit regional GPS data with a viscoelatic model and find $3\ mm \cdot yr^{-1}$ of shortening perpendicular to the PA-SNGV relative plate velocity. *Savage et al.* [2004] prefer an interpretation where there is uniform contraction across the entire Coast Range. The U.S.G.S. collected additional campaign GPS observations since the publication of those papers and the reduced scatter in the data allow more reliable constraints on the magnitude of convergence and the area over which it is accomodated. Here we discuss those new results along with observations further south in the Bay Area.

Several of the previous observations of convergence in the Coast Range were based on the presentation and interpretations of profiles across the plate boundary, such as we show for BĀVŪ in Fig. 1.13 [e.g., Fig. 2 of *Murray and Segall*, 2001; Fig. 5 of *Prescott et al.*, 2001; Fig. 4 of *Savage et al.*, 2004]. These plots show the two horizontal components of GPS velocity projected onto a coordinate system with axes parallel and perpendicular to an "average" plate boundary orientation (usually parallel to the PA-NA relative motion and not PA-SNGV). The shape of the profile is highly dependent on the choice of the orientation used to define this average. Because the deformation field is projected onto a single orientation, pure strike-slip motion on faults with a range of orientations can yield an apparent "fault normal contraction" signal. Figure 1.14 shows GPS data from the North Bay profile perpendicular to the San Andreas fault (N33.85W, Fig. 1.14a) and the azimuth of maximum shear strain from *Savage et al.* [2004] (N29.4W, Fig. 1.14b). When accounting for the formal uncertainties, both profiles are statistically permissive of a scenario with no net convergence. The systematic pattern in both plots, however, implies that the variations are not random scatter. In the first profile, there is an abrupt step in the data at the Green Valley fault, suggesting $\sim 2\ mm \cdot yr^{-1}$ of contraction between the Pacific and SNGV accommodated near that structure. In the latter example, there is no net plate-boundary

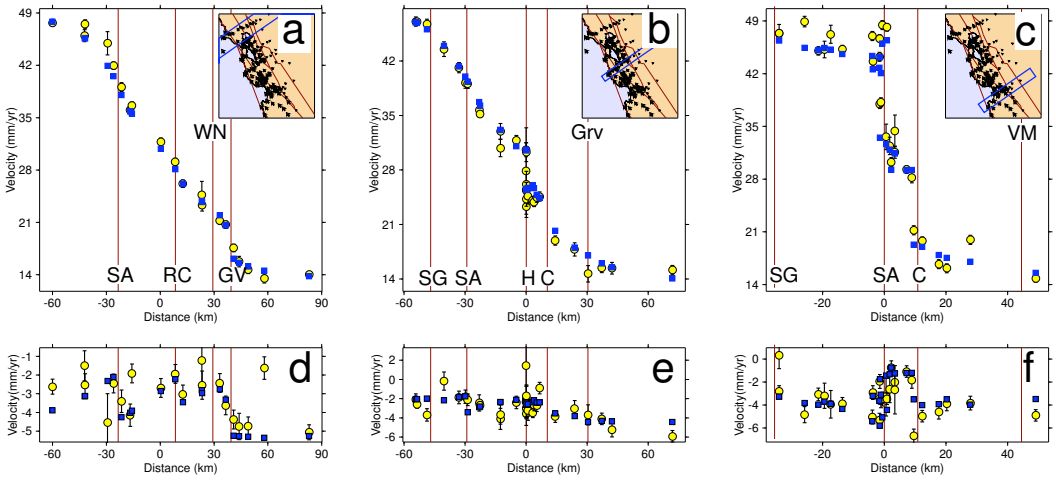

Figure 1.13. Profiles of GPS velocities along profiles perpendicular to the San Andreas fault system. Top panels show the component of the velocity parallel to N33.85W, the approximate strike of the San Andreas fault in the Bay Area. Bottom panels show component of velocity perpendicular to N33.85W. Circles are observations with 1σ uncertainties. Squares are model fit from our Preferred model. For each profile, we include velocities within the box shown in the inset map.

normal motion between the Pacific and SNGV blocks (the data have nearly the same value on both ends of the profile). Within the Bay Area, the systematic triangular shape in Fig. 1.14b suggests localized contraction across the Green Valley fault balanced by a broader zone of extension of equal magnitude west of the Rodgers Creek fault. These two different projections of the same data yield different conclusions about the magnitude and location of convergence in the Bay Area – even though the profile orientation differs by only 4.5°. This comparison should emphasize the hazard of representing spatially complex 2-D velocity data in an essentially 1-D illustration. Evidence for convergence cannot come from these "plate-boundary perpendicular" profiles.

More precise and rigorous measurements of the convergence across individual Bay Area faults comes from comparing the vector representing the relative motion between blocks and the orientation of individual faults accommodating that motion. Faults that are perfectly parallel to the relative motion vector will have pure strike-slip motion. *Argus and Gordon* [2001] present a detailed comparison of mapped fault strikes with predicted relative velocities between the Pacific and SNGV blocks and we present a similar analysis here. Figure 1.15 shows the orientation of PA-SNGV and PA-NA relative motion in central California derived from the rotation axes in our Preferred model. Note how the relative motion of the blocks is close to parallel at the southern end of the SNGV block and becomes less and less parallel further to the north. If the Bay Area is influenced in any way by the relative motion between PA-NA, this interaction would be more easily identifiable in the northern part of California where the PA-NA relative motion differs most from the PA-SNGV motion. Lacking geodetic data within the Bay Area, *Argus and Gordon* [2001] use a comparison

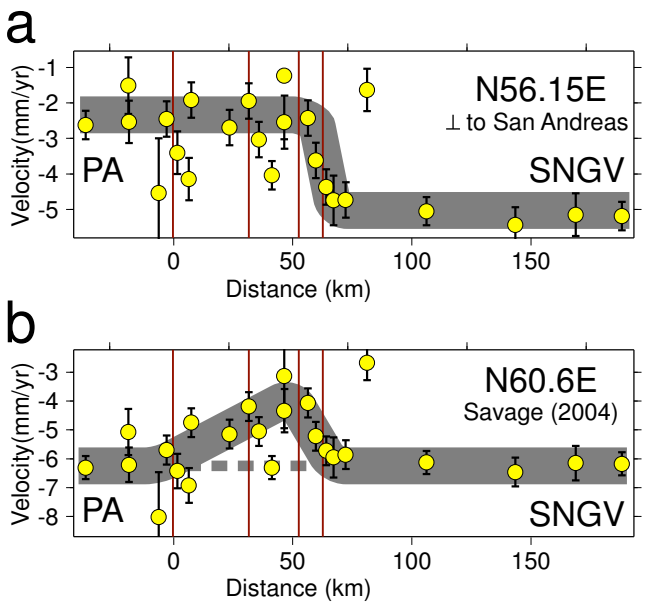

Figure 1.14. Effect of profile orientation on conclusions about convergence. Top panel here is the same as the bottom panel of Fig. 1.13a showing the profile-perpendicular component of velocities from the northern Bay Area along a profile at N56.15E, perpendicular to the strike of the San Andreas fault. Bottom panel shows profile-perpendicular velocities projected onto a slightly different orientation, N60.6E [the orientation of maximum extension from *Savage et al.*, 2004]. The orientation perpendicular to PA-SNGV motion at this latitude from our Preferred model is N59.6E. Thick grey bands show possible interpretations of the data. Dashed line in bottom panel is horizontal for reference. Even though profiles differ by only 4.5 degrees, the apparent convergence between the Pacific and SNGV blocks changes dramatically. Figure inspired by comments of Jim Savage, 2004.

between geologic slip rate estimates on Bay Area faults and their geodetic estimate of PA-SNGV relative motion to estimate the magnitude of fault normal convergence. With our block model, we are able to calculate the relative motion vector for individual blocks within the Bay Area directly. The yellow vectors in Fig. 1.15 show the orientation and magnitude of relative motion that is accommodated by faults in our Preferred model. For the vectors, we hold the eastern side of each fault fixed. They show that relative motion is, in general, nearly parallel to local fault strike. Resolving these vectors onto the local fault orientation indicates how much convergence must be accommodated. These results are reported as "tensile-slip rates" in Table 1.8. The bend in the San Andreas fault at the the Santa Cruz Mountains shows as much as $4.9 \pm 0.6\ mm \cdot yr^{-1}$ of contraction perpendicular to the segment (likely accommodated by a number of thrust faults alongside the San Andreas fault). In general, motions east of the Bay are slightly clockwise of the faults, indicating convergence across the block boundaries, which is balanced by a slight extensional component west of the Bay. The magnitude of convergence increases from $0.1 \pm 1.0\ mm \cdot yr^{-1}$ along the northern Hayward fault to $1.1 \pm 1.0\ mm \cdot yr^{-1}$ on the southernmost creeping segment of the Hayward fault (Hayward_3). The segment connecting the Hayward and Calaveras faults that roughly parallels the seismicity beneath Mission Peak (Hayward_South) has $3.0 \pm 1.0\ mm \cdot yr^{-1}$ of convergence. Along the eastern margin of the Coast Range, the Valley Margin deformation zone converges by $2.7 \pm 0.8\ mm \cdot yr^{-1}$. The Concord/Green Valley system requires a similar magnitude of convergence, but is located so close to the West Napa fault that the elastic model would probably not be able to distinguish between deep tensile-slip on the two faults. We therefore treat the Concord/Green Valley and West Napa fault systems together and find $1.9 \pm 3.0\ mm \cdot yr^{-1}$ of convergence. The San Gregorio fault and Marin segment of the San Andreas fault both show extension, with 2.9 ± 0.6 and $1.9 \pm 0.6\ mm \cdot yr^{-1}$, respectively. It is not possible to determine if this motion is accommodated onshore or offshore because of the sparse data west of these faults. Either way, this slight extension is required to satisfy the total PA-SNGV relative motion. We therefore agree with the assertion by *Savage et al.* [2004] that there is minimal net convergence across the Bay Area.

While thrust faulting parallel to the major faults is likely to accommodate much of the "convergence" implied by the relative motion vectors of some faults in the system, we note that it is possible for strike-slip faults to carry all of the relative motion if they are oriented correctly. This caveat is analogous to the discussion of profile orientation in the previous paragraph. When calculating the magnitude of fault-normal displacements, it is essential to know the orientation of the structure that will be accommodating that motion.

A Note about Block Modeling

The fault-normal slip rates from some previously published block models are sometimes of larger magnitude than geologically inferred slip rates [e.g., *McClusky et al.*, 2001; *Meade et al.*, 2002]. From our own modeling, we find this is especially true when faults are separated by horizontal distance less than a few locking depths and there is limited GPS data on the blocks. The inversion assigns high fault-normal slip rates of opposite signs to pairs of faults that are located close to one another. In such cases, the total fault-normal slip satisfies the far-field constraints well because the large convergence on one fault is balanced

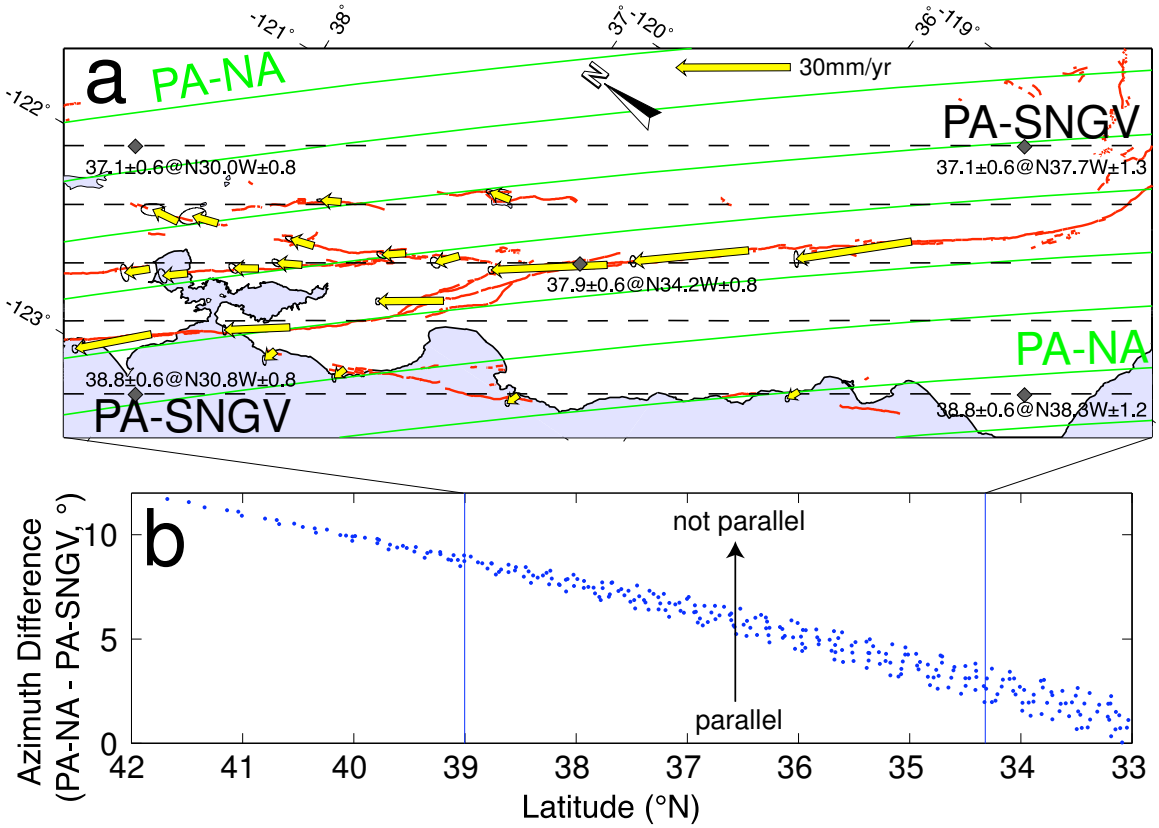

Figure 1.15. a) Calculated orientation of relative motion for PA-NA (light colored, solid curves) and PA-SNGV (black, dashed horizontal lines) based on rotation axes from our Preferred model. Map projected about the PA-SNGV pole so that fault segments and velocities parallel to the PA-SNGV relative motion show up as horizontal. Velocity vectors with error ellipses are the relative motion vector accommodated by each fault at the given location, assuming that the northeastern side of the fault (top of figure) is held fixed. Vectors parallel to fault indicate pure strike-slip motion. Because the eastern block is fixed on these dominantly right-lateral faults, vectors with azimuths clockwise of their respective fault segment indicate convergence and vectors trending counterclockwise represent divergence. In general, note that faults nearer to the top of the figure tend to show more convergence while those near the bottom of the page show a slight divergence. Filled diamonds with labels are PA-SNGV rate in $mm \cdot yr^{-1}$ and azimuth at select locations. b) Difference in azimuth between the PA-NA and PA-SNGV relative motion vectors for points on a regular grid spaced throughout the map above. The two differ in azimuth by only 2° at the south end of the map and almost 8° at the north end. Note that this graph extends further north and south beyond the Great Valley to accentuate the trend of the line and show that the two relative velocities become parallel just south of the Great Valley. The parallel motions would theoretically allow pure transform faulting to accommodate all of the relative motion across southern California if the Great Valley extended south to a latitude of 33°N.

by an equally large extension on a neighboring fault. *Meade and Hager* [2004] refer to this phenomenon as "checkerboarding." We found through trial and error that constraining the inversion to minimize the fault-perpendicular component on a very small number of segments reduces these slip rate oscillations throughout the entire model. We add an *a priori* constraint to the fault perpendicular slip rate on three segments whose strike is within 2.5° of the orientation of the PA-SNGV relative motion (northernmost Calaveras, northern Greenville, and northern Concord). We use a value of $0 \pm 3\ mm \cdot yr^{-1}$ for this constraint. These 1σ error bounds should allow convergence up to the total rate implied by previous geodetic studies for the entire Bay Area to occur on these three segments if the data actually require it. We apply an identical constraint to the Paicines fault because of its extremely close proximity to the much larger San Andreas fault. All other segments in the model are unconstrained. Adding these constraints increases the total χ^2 by 0.5%, but improves the χ^2/DOF because the constraints reduce the number of degrees of freedom. The constrained model does not cause a statistically significant change in any of the model estimates. Figure 1.12 shows the difference between our Preferred model (with the constraint) and an identical geometry without the constraint ("Preferred, Unclamped"). The blank map indicates that the two produce an almost identical residual velocity field and that there are no localized degradations to the model fit. We feel that the model with these loose constraints produces physically reasonable slip rates without compromising the model fit or changing the qualitative interpretation of the results.

1.6.4 Implications for fault system development

What does the systematic progression of poles of rotation from west to east shown in Fig. 1.8 tell us about the evolution and behavior of the Bay Area faults? There are two possibilities: 1) The rotation axes reflect the existing geometry of the faults. Blocks merely move in a manner that is kinematically and mechanically favorable, given the orientation of pre-existing weaknesses in the area. Or, 2) Active faults are oriented at an optimal angle to the far-field motion of the plates that drive them (to produce pure strike-slip faulting, for example) [*Wesnousky*, 1999]. Faults that are less optimally oriented might be abandoned over time. Distinguishing the relative contributions of these two end-member processes is beyond the scope of this work, but we can discuss the latter option that fault orientation reflects the orientation of present-day plate motion. Some faults in the Bay Area such as the San Andreas are oriented parallel with present day PA-NA motion, despite the fact that the plate boundary that should exert a controlling influence on the Bay Area is between the Pacific and SNGV blocks [e.g., *Argus and Gordon*, 2001, ; W. Lettis, pers. comm., 2004]. Such an observation might imply that the orientation of these faults could be inherited from a time when the SNGV block moved more closely with North America. Figure 1.15a shows the geometry of the San Andreas fault system compared with small circle traces parallel to the relative motion of the PA-NA and PA-SNGV. Faults that accommodate pure strike-slip motion between the PA-SNGV show up as horizontal lines in this map projection. Few, if any, of the faults in the Bay Area are horizontal over much of their extent. Most notably, almost the entire San Andreas fault is rotated counter-clockwise by $\sim 5°$ from the ideal PA-SNGV motion (with the Santa Cruz Mountains segment rotatated $> 20°$

away). It is, in fact, roughly parallel with the predicted PA-NA motion from our Preferred model. The central Calaveras, central Greenville, Concord, and Ortigalita faults have strikes approximately parallel to PA-SNGV motion. Other fault segments, such as the southern Calaveras, the Green Valley, and San Gregorio faults strike as much as 10° clockwise of the present PA-SNGV motion. With the exception of the San Gregorio fault, faults striking parallel to or clockwise of PA-SNGV motion are east of the Bay. The general disagreement between fault strike and total plate-boundary motion suggests that present-day plate motion cannot explain the orientation of active faults in the Bay Area. *Wakabayashi* [1999] shows a general progression where the oldest active faults in the Bay Area initiated in the west while the youngest faults in the Bay Area are to the east (though he emphasizes that there are abundant exceptions to this trend, especiallly for faults that appear to have been abandoned and are currently inactive that show a much more complex age distribution). We focus here on the active faults because those are the ones that are relevant for rotation axes derived from active deformation measurements. Figure 1.16 explores the relationship between the orientation of plate motion in the past and the timing of initiation for individual fault segments. We calculate the PA-SNGV motion by subtracting the Basin and Range motion [reference point 'A', *Wernicke and Snow*, 1998] from PA-NA motion [*Atwater and Stock*, 1998]. The exact timing of initiation for many of the faults is not constrained reliably enough to make any definitive conclusions from this figure. However, the plate reconstructions emphasize that the relative motion between PA-SNGV has rotated by $> 30°$ during the lifetime of many Bay Area faults, and that this range encompasses most of the range of fault strikes observed in the Bay Area. In light of these dramatic changes in plate motion in the past, it is probably unwise to make conclusions about fault system development from our present-day GPS-derived rotation axes.

1.6.5 Fault Connections

Calaveras-Paicines-San Andreas

Maps of Holocene faults show the Paicines fault running parallel to the San Andreas for about 50 km [*Jennings*, 1994]. These maps show no Holocene connection between the San Andreas and Calaveras/Paicines system. Attempts to exclude the Paicines fault from our models provide very bad fits to the station between the San Andreas and Paicines faults, and the Paicines fault is known to creep at the surface [*Sauber*, 1989; *Galehouse and Lienkaemper*, 2003]. In our Simple and Preferred models, we include the Paicines and connect it to the San Andreas near the southern end of its mapped Holocene trace (segment 10 of Fig. 1.4). In our Complex model, we add a segment extending the southern Calaveras fault to intersect the San Andreas fault (segment 9 of Fig. 1.4). This new segment bounds an independent block between the San Andreas, Calaveras, and Paicines faults and allows more slip to be transferred from the Calaveras-Paicines system to the San Andreas fault. This connection is typically included in models that exclude the Paicines fault [e.g., *Matsu'ura et al.*, 1986], but our Complex model shows that both this connection and the Paicines fault improve the fit to data. The strike-slip rates in the Complex model are $25.6 \pm 3.0\ mm \cdot yr^{-1}$ and $2.2 \pm 0.4\ mm \cdot yr^{-1}$ on the San Andreas and Paicines faults, respectively.

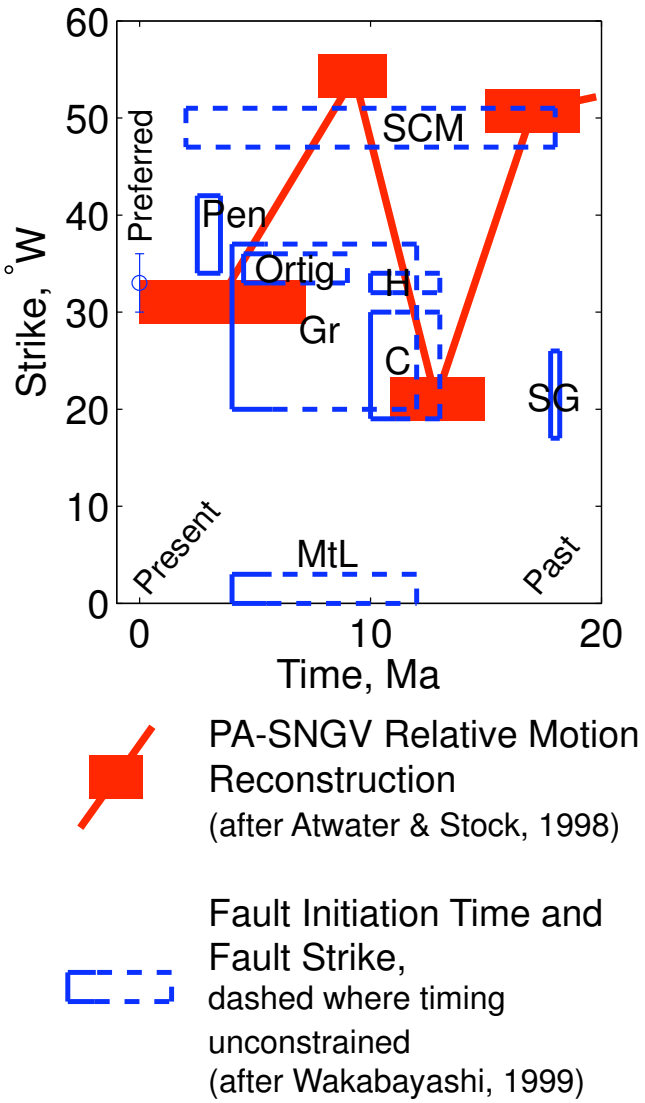

Figure 1.16. Comparison of the present-day strike of Bay Area faults (open rectangles) with the orientation of relative motion between the Pacific and SNGV blocks (filled rectangles and line connecting them). Fault abbreviations: C, Calaveras; Gr, Greenville; H, Hayward; MtL, Mt, Lewis; Ortig, Ortigalita; Pen, Peninsula segment of the San Andreas; SCM, Santa Cruz Mountains segment of the San Andreas; SG, San Gregorio. Fault initiation times come from *Wakabayashi* [1999], and are dashed where loosely constrained. For example, the San Gregorio fault's initiation is well constrained, but the Mt. Lewis fault could have initiatied as early as 12 Ma (dashed right edge of box) and must have iniated by 5 Ma (solid left edge of box). Height of open box represents range of fault strikes for the given fault. Relative motion is reconstructed in the geologic past by *Atwater and Stock* [1998] (PA-NA) and *Wernicke and Snow* [1998] (SNGV-NA). They report average rates over the given time interval indicated by the width of the solid bars. The height is arbitrary because no uncertainty is reported. Circle with error bars at present day shows relative motion calculated from our Preferred model.

Northern Calaveras

The northern termination of the mapped Calaveras fault is an area where there is still significant debate about which faults are connected to each other and where slip on the Calaveras gets transferred after the mapped Calaveras fault terminates. *Galehouse and Lienkaemper* [2003] argue that nearly identical surface creep rates on the two systems implies that the Calaveras connects eastward to the Concord-Green Valley fault via a mechanically favorable releasing step. Others [*Unruh and Lettis*, 1998; *Unruh et al.*, 2002] argue that fold and fault geometry in the East Bay Hills requires that the Calaveras steps westward with a restraining geometry, connecting to the West Napa fault and eventually transferring slip to the Rodgers Creek fault somewhere north of San Pablo Bay. Determining how slip is distributed between faults in the northern East Bay has important implications for the seismic hazard in these growing suburban areas. Using our block model, we focus on this junction and test a wide range of model geometries.

Overall, there is no significant difference between models where the Calaveras steps east versus west, though there are some scenarios where the east-stepping model produces a slightly smaller model misfit. Here we describe the effects of the two models "CalaverasWest" and "CalaverasEast," which are both based on the Preferred model.

Forcing the Calaveras to transfer all slip to the west (CalaverasWest) decreases the distance between the Calaveras and Hayward/Rodgers Creek systems. The deformation gradient in the GPS data near these two fault systems limits the combined slip that can be accommodated by deep locked faults. When the two fault systems are close together, there is a tradeoff where more slip on the Calaveras/West Napa system requires less slip on the Hayward/Rodgers Creek system. Slip on the Hayward fault in the CalaverasWest model is $5.2 mm \cdot yr^{-1}$, well below the $\sim 9\ mm \cdot yr^{-1}$ geologic slip rate estimated from offset stream channels. The total misfit and χ^2/DOF of the CalaverasWest model is higher than the CalaverasEast and Preferred models, though not substantially higher. Compared to the Preferred model, the χ^2/DOF is 2.0% higher, but CalaverasWest affects the fit to stations as far away as Parkfield (Fig. 1.12).

CalaverasEast produces a higher slip rate on the Hayward fault of about $7.5 mm \cdot yr^{-1}$, but also allows for $10.0 mm \cdot yr^{-1}$ on the Green Valley fault because the Green Valley fault carries slip from both the northern Calaveras fault and the Valley Margin deformation zone. The χ^2/DOF of the CalaverasEast model is 0.8% higher than the Preferred model and only affects the fit to GPS data in the northern Bay Area near where the model geometry differs.

Our Preferred model allows Calaveras slip to transfer both east and west. In it, slip rates are about half-way between the two scenarios CalaverasWest and CalaverasEast. Other model geometries that include the Mount Lewis trend, exclude the Valley Margin deformation zone, or use slightly different fault geometries have similar results.

Despite the fact that there are a number of GPS stations in the area of interest, it may never be possible to distinguish between these different scenarios using geodetic data alone. The West Napa and Green Valley faults are located < 10 km apart, roughly the same as the geodetic locking depth. It is difficult to distinguish between two elastic dislocations buried about 15 km below the surface and spaced only 10 km apart. The added constraint

from block offset could help distinguish between the two faults, especially as the details of shallow creep on the Green Valley fault are determined more precisely.

Beyond fault connections

While fault connections provide a likely explanation for the variation in slip rate along strike, there are other reasonable explanations that involve additional complexity. Variations in creep rate during transient slip events are common [e.g., *Linde et al.*, 1996] and probably not artifacts of the observations. The modeled slip rate on our segments therefore represents an average over space and time. Similarly, observations of different slip rates on adjacent fault segments could be indicative of deformation that is accommodated by inelastic processes or more complex 3-D kinematics that are not considered in our block model. Both of these explanations would likely produce complex deformation patterns that could not be detected with our GPS data set alone, but would require denser spatial coverage from techniques such as InSAR.

1.6.6 Locking Depth

The transition between creeping and locked behavior may not occur exactly at D_{95}, but we would expect the relative values of D_{95} to reflect the relative depth of this transition. To allow for the uncertainty in the absolute depth of the geodetic transition, we run the model multiple times and shift the locking depths uniformly up and down over a range of average depths. For example, D_{95} for the northern Hayward fault is 12 km and D_{95} for the Concord fault is 16 km. In our model runs, the locking depth of the Hayward fault is always 4 km shallower than the Concord fault, but we evaluate locking depths over the range of 3 - 17 km for the Hayward fault. This uniform vertical shift also allows for the uncertainty in the exact depth of D_{95} because we derive D_{95} from an earthquake catalog where earthquakes are all located precisely relative to one another, but their exact location in space is not known as accurately.

We show model misfit as a function of locking depth in Figure 1.17. The best fit comes when the locking depths are about 5 km shallower than D_{95} for each segment. In model runs where faults are assigned a uniform locking depth, we find similar results. A 8 km uniform locking depth provides the best geodetic fit, even though it is also about 5 km shallower than the average 13 km D_{95} for the entire Bay Area. Locking depths based on D_{95} produce insignificantly better model fit than the best-fitting uniform locking depth, but we prefer them because they are consistent with data outside the model.

Neither the uniform locking depth or deviations from D_{95} represent the absolute best statistical fit to the data. Both approaches shift all locking depths uniformly up or down. Since some of the largest differences between observed and model GPS velocities occur near the San Andreas fault in the southern Bay Area, Fig. 1.17 is dominated by the preference for shallow slip in that area. For example, fixing the locking depth of the Santa Cruz Mountains segment of the San Andreas fault to 5 km and keeping all other locking depths

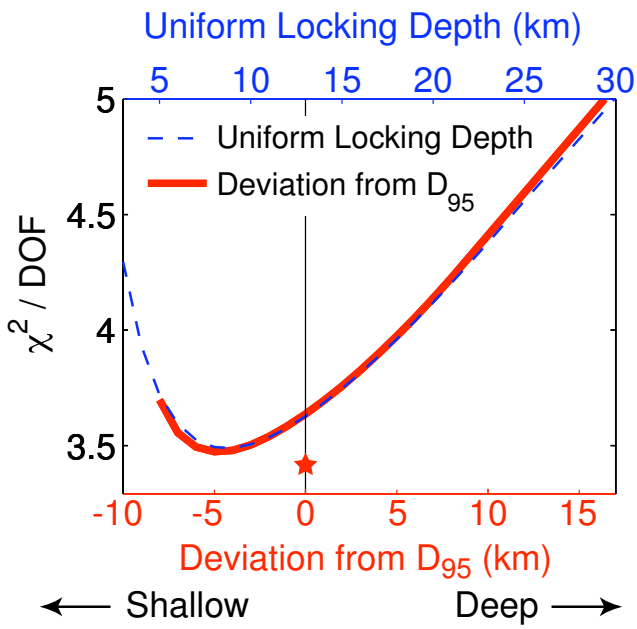

Figure 1.17. Model misfit v. locking depth for the preferred geometry. Uniform locking depth (thin dashed curve, top axis) assigns all dislocations the same locking depth. Deviation from D_{95} (thick solid curve, bottom axis) assumes that locking depths deviate by the amount indicated on the x-axis deeper or shallower than D_{95} for their specific location. Negative values on the x-axis are shallower than D_{95}. For faults with surface creep, the locking depth represents the transition between the deep slip rate and the shallow creep rate. The two curves are almost identical. Solid curve does not extend shallower than -8 because the shallowest locking depths would intersect the surface. Small star at x=0 shows misfit for a model assuming locking depths of D_{95} everywhere except the Santa Cruz Mountains segment of the San Andreas fault where we arbitrarily assign a very shallow locking depth of 5 km. This model gives better fit than uniform locking depth or deviations from D_{95}, highlighting the fact that the greatest misfit to GPS data occurs near that segment.

at D_{95} produces a better model fit than shifting the entire model shallower by 5 km (star, Fig. 1.17). While simultaneously inverting for both locking depth and slip rate would avoid such sensitivity, *Prescott et al.* [2001] found that such joint inversions produce poorer constraints on the slip rate and result in less geologically reasonable slip distributions.

Shallow Creep Transition Depth

Our treatment of shallow aseismic creep is probably oversimplified compared to faults in nature. Distributed slip models of the Calaveras and Hayward faults show a general pattern of high aseismic slip rates near the surface with locked patches (very low aseismic slip rates) extending from a few kilometers depth to the seismic-aseismic transition (LD) [*Manaker et al.*, 2003; *Schmidt et al.*, 2004]. While the spatial resolution of our GPS data is not high enough to constrain the fine details of the aseismic slip distribution, we can explore the general distribution of slip within three depth intervals along creeping faults: 1) a shallow dislocation representing aseismic creep from the surface to some depth, TD; 2) a locked patch between the depths of TD and LD; and 3) a deep dislocation below LD. In the models considered thus far, we assumed that TD=LD, resulting in only two depth intervals along the fault (1 and 3 from above). Here we evaluate a variation on the Preferred model where TD is a fixed depth of 5 km on all creeping faults, representing shallow creep restricted to the upper 5 km (Model "Preferred, TD=5"). The χ^2/DOF is 6% higher in "Preferred, TD=5" compared to the Preferred model. Slip rates for TD=5 are almost all within the 95% confidence limits of the Preferred model, but there are some notable differences. The shallower TD produces less slip at intermediate depths, so slip rates on the remaining dislocations must be higher to yield the same surface deformation. The resulting shallow slip rate is universally faster than for cases where TD=LD. For the Hayward fault where the data constrain the shallow creep very well, the increase is $< 0.2\ mm \cdot yr^{-1}$. For creeping segments of the San Andreas and Calaveras faults, the shallower TD produces slip rates 1-2 $mm \cdot yr^{-1}$ faster than when TD=LD. By assuming TD=5, the deep strike-slip rate on the central Calaveras fault increases from 12.9 to 15.0 $mm \cdot yr^{-1}$ and the slip on the Hayward fault increases from 6.5 to 6.9 $mm \cdot yr^{-1}$. These slip increases are balanced by a decrease of slip on several of the other Bay Area faults such that the total slip across the entire Bay Area differs by less than 0.3 $mm \cdot yr^{-1}$ as TD varies. The San Gregorio and Greenville faults both have decreased slip rates (drops of 0.6 and 1.2 $mm{\cdot}yr^{-1}$, respectively). We find similar results in a model where the shallow creep transition is exactly half-way between D_{95} and the surface (Model "Preferred, TD=$D_{95}/2$").

This relative insensitivity to the shallow creep transition depth is similar to the findings of *Thatcher et al.* [1997] who describe a geodetic inversion of slip during the 1906 earthquake. Aseismic creep and coseismic slip are modeled using identical dislocations – they differ only in the time scale over which they occur. *Thatcher et al.* [1997] find that varying the depth extent of dislocations from 5-20 km causes <20% difference in the calculated slip on those elements. They also emphasize that even though the calculated slip is uniform along the entire dislocation, the inversion is more sensitive to the slip rate in the shallow portions of the fault that are closer to the surface geodetic data.

We employ the assumption that TD=LD in our Preferred model because it produces the lowest χ^2/DOF. The improved fit may be due to the fact that slip rates between TD and LD are not exactly zero for the natural faults and that TD is likely to vary widely among the faults considered. By exploring a range of TD, we find that the shallow creep rates in our Preferred model are a lower bound, and the deep slip rates may vary from the Preferred model by $1-2\ mm \cdot yr^{-1}$ for more complex distributions of shallow slip.

1.6.7 Comparison With Long Term Slip Rates

Numerous geologic investigations have determined long term average slip rates for Bay Area faults during portions of the Holocene. Such studies provide essential input into earthquake hazard assessment and an comprehensive summary of previous work has been compiled for this purpose [Chapter 3 of *Working Group on Northern California Earthquake Probabilities*, 2003, "WG03"]. In general, the geodetically observed slip rates agree well with the values from WG03 (Table 1.7). Slight differences could reflect a combination of errors in each of the data sets or a real difference in the behavior of faults during the last decade compared to the last several thousand years. Both the Greenville fault and the Green Valley/Concord fault system have slip rates higher than preferred bounds from WG03. More recent paleoseismological work by *Sawyer and Unruh* [2002] constrains the slip rate on the Greenville fault to $4.1 \pm 1.8\ mm \cdot yr^{-1}$. Our Preferred model is $1.3\ mm \cdot yr^{-1}$ higher, but now within the error bounds. The northern San Gregorio fault and Marin segment of the San Andreas fault both have slip rates lower than the preferred bounds. The Hayward fault, Calaveras fault, and San Andreas fault from the Peninsula south all have slip rates within the bounds described by the working group, but slightly lower than the most probable value. WG03 does not explicitly consider the effects of the West Napa fault as a possible extension of the Calaveras fault, while we find a slip rate of $\sim 3.5\ mm \cdot yr^{-1}$. We find a strike-slip rate for the Valley Margin deformation zone of $5.4 \pm 1.0\ mm \cdot yr^{-1}$ in our Preferred model. WG03 does not estimate a slip rate for this region, but geologic investigations by *Anderson and Piety* [2001] show that the northern Ortigalita fault carries 0.5-2.5 $mm \cdot yr^{-1}$ of slip. The slip rate across the entire eastern Coast Range must be at least as high as the rate for this single structure.

To test if the preferred WG03 fault parameters (long-term slip, fault width, and shallow locking ratio, R) are compatible with the BĀVŪ geodetic data, we apply these parameters as *a priori* constraints on our preferred model geometry. Running the inversion with these constraints produces very poor model fit (χ^2/DOF of 29.8). Where geodetic data are sparse, the inversion relies very strongly on the *a priori* slip rates. On the San Gregorio fault, WG03 uses a high slip rate ($7 \pm 3\ mm \cdot yr^{-1}$) on the northern section and a lower rate ($3 \pm 2\ mm \cdot yr^{-1}$) further south. Since the weight of the *a priori* constraints overwhelms the sparse data in the area, the inversion fits this slip gradient by imposing an internal rotation of the Santa Cruz block. The rotation requires almost 20 $mm \cdot yr^{-1}$ of deep fault-normal slip on the San Gregorio fault, which must then be balanced by nearly equal and opposite displacements on other Bay Area faults in order to satisfy the regional block motion that have minimal total convergence across the Bay Area. We can avoid this highly unrealistic scenario by removing the slip rate constraints on both segments and allowing the geodetic

data alone to dictate the slip rate. That model ("Preferred, WG03") has χ^2/DOF of 9.6 and slip rates of 5.8 and 7.0 $mm \cdot yr^{-1}$ on the northern and southern segments, respectively. The misfit from our best WG03-based model is more than twice that of our Preferred model.

1.7 Conclusions

The interseismic velocities at over 200 Bay Area stations make BĀVŪ the most comprehensive picture of crustal deformation in the region compiled to date. We show that the block modeling approach enables us to interpret these velocities at an unprecedented range of spatial scales.

We constrain the motion of blocks in the Bay Area relative to adjacent global plates (North America and Pacific), as well as the SNGV microplate. Individual blocks within the Bay Area do not move about identical poles of rotation of any of these major blocks as a "perfect transform" system, but instead have poles at intermediate locations. The poles transition systematically from west to east (Fig. 1.8). This systematic pattern may have implications for the development of the fault system, though we show that the present-day relative plate motions cannot explain the configuration of most Bay Area faults.

Looking at the Bay Area region itself, we focus on quantifying the slip rates of individual faults. We use precise relocations of earthquakes to determine the maximum depth of seismicity as a proxy for the local seismic/aseismic transition. We find slip rates that are typically within the uncertainty of geologic estimates (Table 1.7). We also document substantial slip on segments that have not been emphasized in previous studies. Models that include up to 4 $mm \cdot yr^{-1}$ of strike-slip on the West Napa fault north of San Pablo Bay provide almost identical model fit to those that exclude this fault. In our Preferred model, we favor this geometry because it is consistent with geologic evidence showing that the some slip from the Calaveras fault is transferred westward, eventually connecting to the West Napa fault system. Adding a fault along the eastern margin of the Coast Range in our Preferred model produces lower misfit and a geologically reasonable slip sense (right-lateral) on the Greenville – a notable improvement over models that exclude this "Valley Margin" deformation zone. This fault, running parallel to the San Andreas through central California carries ~ 5 $mm \cdot yr^{-1}$ of right-lateral slip and 3 $mm \cdot yr^{-1}$ of fault-normal convergence. Poor data coverage near the model fault segment prevent us from determining if the deformation is accommodated by a single structure or a broad zone with many structures as might be implied by the distribution of moderate thrust earthquakes within the Diablo and Coast Ranges. We find that a similar magnitude of convergence is preferred along the entire eastern front of the Coast Range, but that an equal and opposite extension is observed west of the Bay in our models. Our block modeling approach provides the first strong geodetic constraints on the slip rates of several other faults because we include global GPS data from the Pacific plate and the physical constraint of coherent block motion. These faults include the San Gregorio fault (2.4 ± 0.5 $mm \cdot yr^{-1}$ right-lateral slip rate) and the Mount Diablo thrust (3.9 ± 0.5 $mm \cdot yr^{-1}$ reverse slip and an almost equal magnitude of right-lateral

strike-slip). Overall, we find that the slip rates we determine fit GPS data substantially better than the slip rates defined in WG03.

Locally, block modeling allows us to test the connectivity of faults. Faults that are connected can transfer slip, so these connections have implications for slip rates and seismic hazard assssment. We show that shallow creep on Paicines fault is important, but that deep slip is best modeled when the Calaveras fault is directly connected to both the Paicines and San Andreas faults. East of the Bay, we explore the possibility that the northern Calaveras fault transfers its slip east to the Concord/Green Valley fault, west to the West Napa fault system, or a combination of the two. The data slightly favor the eastern step over the western step alone, but we prefer models where both connections are included because they most closely reproduce the geologically inferred slip rate on the Green Valley fault and the lowest total model misfit.

In block modeling, three-dimensional fault geometry and connectivity have a very strong impact on the interpretation of surface deformation. While we systematically explored an extremely wide range of model geometries in this work, we look forward to further geologic constraints on fault geometry in 3-D to improve the reliability of block models. The ability to iteratively explore these different block geometries and test their consistency with geodetic data make the block modeling approach an excellent tool for understanding fault kinematics in the Bay Area.

Table 1.5. Vectors representing axes of relative rotation from various studies.

Reference	**Lon** ^oE	**Lat** ^oN	**Rate** $^oMyr^{-1}$	$\sigma_{\mathbf{1}}$[a] ^{o}	$\sigma_{\mathbf{2}}$[a] ^{o}	θ[a] ^{o}	$\sigma_{\mathbf{rate}}$[b] $^oMyr^{-1}$
North America - Pacific – Other Studies							
NUVEL-1A[c]	-78.2	48.7	0.749	1.3	1.2	-61	0.012
DeMets and Dixon [1999] Geologic	-76.1	50.0	0.777	0.8	0.6	65	0.007
Larson et al. [1997]	-84.3	49.6	0.83	2.0	1.0	94	0.02
Bennett et al. [1999]	-78.5	49.9	0.78				
DeMets and Dixon [1999] GPS	-73.7	51.5	0.765	2.0	1.0	-85	0.016
Kogan et al. [2000]	-78.7	50.5	0.74				
Murray and Segall [2001]	-78.2	48.7	0.774				$^{+0.007}_{-0.043}$
Miller et al. [2001]	-77.7	50.9	0.78				
Beavan et al. [2002]	-75.0	50.3	0.773	0.4	0.2	94	0.005
Sella et al. [2002]	-72.1	50.4	0.755	0.6	0.4	-79	0.004
Gonzalez-Garcia et al. [2003]	-77.0	49.9	0.766	0.25	0.17	94	0.007
Kreemer et al. [2003]	-77.8	50.8	0.77				
Steblov et al. [2003] (Preferred)	-75.6	50.8	0.777	0.6	0.4	109	0.007
Steblov et al. [2003] 2	-75.1	50.1	0.780	0.6	0.4	109	0.007
North America - Pacific – This Study							
TWOPLATE (Global Sites Only)	-73.9	52.1	0.773	0.5	0.2	94	0.003
SIMPLE	-74.88	51.79	0.770	0.4	0.1	95	0.003
PREFERRED	-74.65	51.85	0.770	0.4	0.1	95	0.003
COMPLEX	-74.16	51.89	0.771	0.4	0.1	95	0.003
CalaverasEast	-74.69	51.85	0.770	0.4	0.1	95	0.003
CalaverasWest	-74.59	51.76	0.770	0.4	0.1	95	0.003
Preferred, Thrust	-74.65	51.84	0.770	0.4	0.1	95	0.003
Preferred, Unclamped	-74.65	51.85	0.771	0.4	0.1	95	0.003
Preferred, LD=$D_{95} - 8$	-76.28	51.80	0.761	0.3	0.1	91	0.003
Preferred, LD=$D_{95} - 5$	-75.61	51.80	0.764	0.3	0.1	93	0.003
Preferred, LD=$D_{95} + 5$	-73.98	51.86	0.776	0.4	0.1	97	0.003
Preferred, TD=5	-74.70	51.86	0.770	0.4	0.1	95	0.003

Table 1.5. (continued) Vectors representing axes of relative rotation from various studies

Reference	**Lon** ^oE	**Lat** ^oN	**Rate** $^oMyr^{-1}$	$\sigma_{\mathbf{1}}$[a] ^{o}	$\sigma_{\mathbf{2}}$[a] ^{o}	θ[a] ^{o}	$\sigma_{\mathbf{rate}}$[b] $^oMyr^{-1}$
Sierra Nevada/Great Valley - North America – Other Studies							
Argus and Gordon [1991]	-128	32	0.61	6	1	51	0.15
Hearn and Humphreys [1998]	-154.4	-13	0.13				
Dixon et al. [2000]	-138.6	19.1	0.243	30.7	2.1	34	0.218
Murray and Segall [2001]	-90.1	53.9	0.208	~ 180			$^{+280}_{-113}$
Sierra Nevada/Great Valley - North America – This Study							
SIMPLE	-139.61	10.71	0.242	5.2	2.9	28	0.040
PREFERRED	-137.41	9.54	0.231	7.6	3.6	25	0.054
COMPLEX	-138.11	8.51	0.224	8.2	3.9	25	0.054
CalaverasEast	-142.47	-0.01	0.176	12.0	5.6	25	0.044
CalaverasWest	-130.65	24.05	0.435	1.7	1.1	30	0.053
Preferred, Thrust	-137.65	9.24	0.228	7.8	3.7	25	0.054
Preferred, Unclamped	-137.52	8.54	0.226	8.1	3.7	24	0.054
Preferred, LD=$D_{95} - 8$	-174.17	-46.17	0.129	21.7	18.3	39	0.006
Preferred, LD=$D_{95} - 5$	-156.03	-25.06	0.133	20.7	12.4	28	0.019
Preferred, LD=$D_{95} + 5$	-129.42	24.32	0.450	2.1	1.2	26	0.067
Preferred, TD=5	-135.60	13.44	0.259	5.9	2.9	25	0.056
Sierra Nevada/Great Valley - Pacific – Other Studies							
Dixon et al. [2000]	-94.6	46.7	0.930	6.5	0.7	78	0.227
Sierra Nevada/Great Valley - Pacific – This Study							
SIMPLE	-95.32	46.50	0.896	1.5	0.3	74	0.044
PREFERRED	-93.86	46.36	0.890	2.2	0.4	76	0.059
COMPLEX	-93.28	46.54	0.882	2.2	0.4	76	0.060
CalaverasEast	-91.43	46.91	0.829	2.4	0.3	78	0.055
CalaverasWest	-99.85	45.36	1.099	1.2	0.3	70	0.053
Preferred, Thrust	-93.78	46.39	0.887	2.2	0.4	76	0.059
Preferred, Unclamped	-93.67	46.29	0.885	2.2	0.4	77	0.060
Preferred, LD=$D_{95} - 8$	-87.18	47.26	0.688	2.9	0.3	82	0.048
Preferred, LD=$D_{95} - 5$	-89.14	47.06	0.744	2.7	0.3	80	0.052
Preferred, LD=$D_{95} + 5$	-99.35	45.29	1.120	1.5	0.4	72	0.066
Preferred, TD=5	-94.92	46.24	0.922	2.0	0.4	75	0.059

Table 1.6. Predicted magnitude of velocity at the Farallon Islands (station FARB) in a fixed North American reference frame. Note that FARB is "slowed" down by $\sim 3\ mm \cdot yr^{-1}$ compared to the total rigid plate motion because of elastic strain along Bay Area faults. FARB is far enough from creeping fault segments to be relatively insensitive to their effect. Studies that ignore strain accumulation are not able to reliably predict the velocity at FARB.

Reference	**Rate** $mmyr^{-1}$	**Azimuth** ^oNW
BĀVŪ *observed*	47.7 ± 0.8	37.0 ± 1.0
NUVEL-1A	46.5	33.5
SIMPLE	48.0	38.4
PREFERRED	48.0	38.5
COMPLEX	48.2	38.5
Variations on models		
CalaverasWest	48.0	38.4
CalaverasEast	48.0	38.3
Preferred, Thrust	48.0	38.5
Preferred, Unclamped	48.0	38.5
Preferred, LD=$D_{95} - 8$	48.2	38.8
Preferred, LD=$D_{95} - 5$	48.2	38.7
Preferred, LD=$D_{95} + 5$	47.7	38.0
Preferred, TD=5	47.9	38.5
Preferred, TD=$D_{95}/2$	47.9	38.5
Preferred, WG03	49.6	38.5
Contributions to Preferred model		
Long-term Block Offset	50.7	38.8
Strain Accumulation	-2.9	47.0
Shallow Creep	0.2	80.1
Sum	48.0	38.5

Table 1.7. Comparison of strike-slip rates for geologic estimates (WG03) and this study. Fault system names from top row: SG, San Gregorio; SA, San Andreas; RC, Rodgers Creek; H, Hayward; C, Calaveras; GV, Green Valley; Gr, Greenville. Fault segments from second row: N, North; C, Central; S, South; Mr, Marin; SF, San Francisco; SCM, Santa Cruz Mountains; RC, Rodgers Creek; H, Hayward; WN, West Napa; Cn, Concord; Gr, Greenville. Total for the northern section includes the sum of SA-Mrn + RC + WN + GV. Southern total is sum of SG-S + SA-SCM + C-C + Gr. We show 95% confidence bounds ($\pm 2\sigma$) for the three main models. Bounds for other models are similar in magnitude.

Model	**SG**		**SA**			**RC/H**			**C**			**GV/Gr**			**Total**	
	N	S	Mr	SF	SCM	RC	H	WN	N	C	S	GV	Cn	Gr	N	S
WG03	7	3	24	17	17	9	9	–	6	15	15	5	4	2	38	37
SIMPLE	1.9	2.6	19.6	16.7	15.6	7.2	7.1	0.0	10.0	17.1	16.2	9.0	8.8	-4.1	35.8	31.2
$\pm$	1.0	0.8	1.4	1.2	0.8	1.4	0.8	0.0	1.6	2.6	0.2	0.6	0.4	1.6	2.1	3.3
PREFERRED	2.4	3.0	20.2	17.1	16.4	6.6	6.5	4.0	6.2	12.9	12.7	7.0	6.7	5.4	37.8	37.7
$\pm$	1.0	0.8	1.4	1.4	1.0	2.4	1.4	3.0	0.8	0.6	0.4	1.8	1.4	0.6	4.5	1.5
COMPLEX	4.9	5.1	20.6	16.0	13.0	7.8	7.6	3.6	4.2	12.4	20.6	6.9	6.5	6.2	38.9	36.7
$\pm$	1.2	0.8	1.4	1.8	3.8	2.4	1.4	3.2	1.0	1.8	2.2	1.8	1.4	0.6	4.6	4.3
Variations on models																
CalaverasWest	2.4	3.0	20.3	17.1	16.1	5.2	5.2	7.4	7.0	12.3	12.0	5.3	5.3	5.3	38.2	36.7
CalaverasEast	2.6	3.1	19.9	16.7	16.2	7.6	7.5	0.0	5.8	13.2	13.0	10.6	10.6	5.3	38.1	37.8
Preferred, Thrust	2.4	3.0	20.1	17.1	16.4	6.6	6.6	4.1	6.4	13.1	12.9	6.9	6.5	5.2	37.7	37.7
Preferred, Unclamped	2.5	3.1	20.1	17.0	16.4	7.0	6.9	2.4	5.7	13.2	12.9	8.3	7.1	5.1	37.8	37.8
Preferred, LD=$D_{95} - 8$	2.5	3.0	17.5	14.5	13.7	6.5	6.5	3.6	6.7	13.2	12.8	7.3	7.0	4.7	34.9	34.6
Preferred, LD=$D_{95} - 5$	2.4	2.9	18.5	15.6	14.7	6.5	6.5	3.7	7.0	13.5	13.1	7.2	6.8	4.6	35.9	35.7
Preferred, LD=$D_{95} + 5$	2.5	3.1	21.1	17.8	17.5	6.9	6.8	5.1	5.0	12.3	12.3	6.2	5.9	6.4	39.3	39.3
Preferred, LD=5	2.7	3.2	16.9	13.8	12.9	7.5	7.5	3.4	6.8	14.2	13.8	6.7	6.4	3.9	34.5	34.2
Preferred, LD=8	2.5	3.1	18.2	15.2	14.3	6.8	6.8	4.2	7.3	14.0	13.6	6.4	6.0	4.1	35.6	35.5
Preferred, LD=13	2.6	3.1	20.1	16.9	16.1	6.3	6.3	5.1	7.0	13.4	13.1	6.1	5.8	4.8	37.6	37.4
Preferred, LD=18	2.8	3.3	21.2	17.7	17.3	6.5	6.4	6.1	6.1	12.8	12.7	5.5	5.2	5.7	39.3	39.1
Preferred, TD=5	1.8	2.3	19.6	17.3	16.6	6.9	6.9	4.9	7.9	15.0	14.7	6.7	6.4	4.2	38.1	38.1
Preferred, TD=$D_{95}/2$	1.8	2.3	19.5	17.2	16.5	7.1	7.1	4.5	7.7	15.0	14.7	6.8	6.5	4.1	37.9	37.9
Preferred, WG03	5.7	7.0	23.8	16.5	16.3	9.2	9.2	1.6	5.1	14.0	14.4	4.2	3.2	3.2	38.8	40.5

Table 1.8. Comparison of tensile-slip rates for calculated from models. Note that positive "tensile-slip" represents contraction and negative values represent extension. See caption of Table 1.7 for abbreviations.

Model	**SG**			**SA**		**RC/H**			**C**			**GV/Gr**		
	N	S	Mr	SF	SCM	RC	H	WN	N	C	S	GV	Cn	Gr
SIMPLE	-3.5	-2.2	-3.2	1.5	6.8	0.3	1.3	0.0	-2.3	4.0	-4.5	0.8	1.4	3.0
±	0.6	0.6	0.6	0.6	0.6	0.8	0.8	0.0	2.0	2.4	0.4	0.6	0.6	2.2
PREFERRED	-2.9	-2.1	-1.9	0.2	4.9	-1.6	0.1	-0.5	1.0	1.1	-3.0	2.4	1.2	-0.4
±	0.6	0.6	0.6	0.6	0.6	1.2	1.0	2.4	0.8	0.8	0.8	1.8	1.8	0.6
COMPLEX	0.0	-0.7	0.2	-4.9	-8.9	-3.3	0.6	-0.5	0.5	4.5	4.7	2.5	1.2	0.3
±	0.8	0.8	0.8	0.8	2.0	1.2	1.0	2.6	1.2	2.2	1.8	1.8	1.8	0.8
Variations on models														
CalaverasWest	-3.2	-1.8	-2.3	1.3	6.3	-2.4	-1.0	3.6	0.7	0.1	-3.3	-0.4	0.8	0.1
CalaverasEast	-2.5	-2.0	-2.3	-0.5	4.4	3.2	2.5	0.0	0.4	1.0	-3.2	-1.2	1.5	-0.3
Preferred, Thrust	-2.9	-2.1	-1.9	0.2	4.9	-1.6	0.0	-0.5	1.0	1.1	-3.1	2.4	1.2	-0.3
Preferred, Unclamped	-2.7	-2.1	-2.0	-0.3	4.5	-1.5	1.1	-2.8	-2.0	0.1	-3.6	4.7	4.7	1.4
Preferred, LD=$D_{95} - 8$	-2.3	-2.0	0.4	1.3	5.1	-0.4	-0.1	-2.4	0.4	-0.3	-3.7	1.5	1.2	-0.2
Preferred, LD=$D_{95} - 5$	-2.7	-2.1	0.2	1.4	5.4	-0.8	-0.2	-3.1	0.6	-0.0	-3.7	2.6	1.2	-0.3
Preferred, LD=$D_{95} + 5$	-3.1	-2.0	-5.8	-2.0	3.8	-1.6	1.0	3.0	1.6	2.7	-2.1	2.3	1.1	-0.3
Preferred, LD=5	-2.2	-1.8	0.6	1.4	5.0	-0.5	-0.3	-3.1	0.3	-0.7	-4.2	2.0	1.1	-0.2
Preferred, LD=8	-2.5	-1.9	0.4	1.5	5.3	-0.6	-0.3	-3.9	0.4	-0.4	-4.0	2.9	1.1	-0.2
Preferred, LD=13	-2.7	-1.8	-1.1	0.7	5.1	-1.0	-0.0	-1.8	0.7	0.5	-3.4	2.6	1.1	-0.3
Preferred, LD=18	-2.8	-1.6	-4.2	-1.2	4.1	-1.4	0.6	1.4	1.3	1.9	-2.7	2.3	0.9	-0.3
Preferred, TD=5	-2.4	-2.0	-1.2	0.1	4.7	-1.9	-0.3	-0.3	1.0	0.8	-3.7	2.0	1.1	-0.4
Preferred, TD=$D_{95}/2$	-2.3	-2.0	-1.3	0.1	4.8	-1.8	-0.2	-0.4	1.0	0.8	-3.7	2.1	1.1	-0.4
Preferred, WG03	-6.6	-4.2	0.7	0.8	1.4	-0.2	1.2	-1.7	8.1	6.8	-0.8	5.4	3.5	-2.6

Table 1.9. Shallow strike-slip ("creep") rates from model. Fault system names from top row: SA, San Andreas; H, Hayward; C, Calaveras; GV, Green Valley. Fault segments from second row: SCM, Santa Cruz Mountains; SJB, San Juan Bautista; Pk, Parkfield; H1-H4, 4 segments from North - South; N, North; Ctl, Central; S1-S2, Southern 1 - 2; nCn, northern Concord; sCn, southern Concord.

Model		**SA**				**H**				**C**			**GV**	
	SCM	SJB	Pk	H1	H2	H3	H4	N	Ctl	S1	S2	nCn	sCn	GV
SIMPLE	9.1	20.6	14.1	4.6	3.9	5.1	4.9	1.5	5.4	14.0	7.8	3.7	3.5	2.7
±	2.0	3.0	4.4	1.4	1.4	1.2	1.6	1.8	6.4	0.8	3.6	1.4	1.2	1.2
PREFERRED	9.0	20.3	13.5	4.5	3.7	5.2	5.2	2.0	8.9	14.0	8.4	3.7	3.5	2.6
±	2.0	3.0	4.2	1.4	1.4	1.2	1.6	1.6	6.2	0.8	3.4	1.4	1.2	1.2
COMPLEX	7.5	20.4	14.3	4.6	3.9	5.3	5.3	1.7	8.9	14.1	6.2	3.8	3.5	2.6
±	2.0	2.8	4.2	1.2	1.4	1.0	1.4	1.8	6.0	0.8	3.4	1.4	1.0	1.0
Variations on models														
CalaverasWest	9.3	20.6	14.0	4.4	3.7	5.2	5.2	2.0	8.9	14.0	8.5	3.8	3.4	2.6
CalaverasEast	9.0	20.3	13.6	4.7	3.8	5.2	5.1	2.2	8.5	14.0	8.4	3.5	3.5	2.7
Preferred, Thrust	9.0	20.3	13.5	4.6	3.7	5.2	5.2	1.8	8.9	14.0	8.3	3.8	3.5	2.6
Preferred, Unclamped	8.9	20.3	13.6	4.6	3.9	5.2	5.3	1.6	8.4	14.0	8.4	3.7	3.5	2.6
Preferred, LD=$D_{95} - 8$	8.9	22.3	-2.3	4.5	3.9	5.2	4.9	1.6	8.6	14.0	6.2	3.9	3.5	2.6
Preferred, LD=$D_{95} - 5$	8.9	20.9	10.0	4.6	3.8	5.2	5.0	1.6	7.7	14.0	7.6	3.8	3.5	2.6
Preferred, LD=$D_{95} + 5$	9.3	20.0	14.7	4.5	3.8	5.3	5.5	2.2	10.3	14.0	8.6	3.7	3.4	2.6
Preferred, LD=5	7.9	21.7	9.9	4.5	3.8	5.2	5.0	1.4	7.7	14.0	7.9	3.9	3.5	2.6
Preferred, LD=8	8.2	21.0	12.4	4.6	3.8	5.2	5.1	1.6	8.2	14.0	8.3	3.9	3.5	2.6
Preferred, LD=13	8.6	20.4	14.0	4.6	3.8	5.2	5.3	2.0	9.4	14.0	8.6	3.8	3.5	2.6
Preferred, LD=18	9.1	20.1	14.7	4.5	3.9	5.3	5.5	2.2	10.7	14.0	8.7	3.8	3.5	2.6
Preferred, TD=5	9.9	22.8	16.5	4.6	3.9	5.3	5.2	2.3	10.2	14.1	8.8	4.0	3.6	2.7
Preferred, TD=$D_{95}/2$	9.9	22.5	16.6	4.6	3.9	5.3	5.2	2.2	10.6	14.1	9.1	4.0	3.5	2.7
Preferred, WG03	7.3	21.3	14.3	5.1	4.0	5.2	6.5	4.0	13.8	12.3	8.3	3.2	4.5	3.7

Bibliography

Altamimi, Z., P. Sillard, and C. Boucher, ITRF2000: A new release of the international terrestrial reference frame for earth science applications, *J. Geophys. Res.*, *107*(B10), doi:10.1029/2001JB000,561, 2002.

Anderson, L. W., and L. A. Piety, Geologic seismic source characterization of the San Luis-O'Neill area, eastern Diablo Range, California, *Seismotectonic Report 2001-2*, Bureau of Reclamation, 2001.

Argus, D. F., and R. G. Gordon, Current Sierra-Nevada North America motion from Very Long Base-Line Interferometry - implications for the kinematics of the western United States, *Geology*, *19*(11), 1085–1088, 1991.

Argus, D. F., and R. G. Gordon, Present tectonic motion across the Coast Ranges and San Andreas fault system in central California, *Geol. Soc. Amer. Bull.*, *113*(12), 1580–1592, 2001.

Arnadottir, T., and P. Segall, The 1989 Loma Prieta earthquake imaged from inversion of geodetic data, *J. Geophys. Res.*, *99*(B11), 21,835–21,855, 1994.

Arnadottir, T., and P. Segall, The 1989 Loma Prieta earthquake imaged from inversion of geodetic data - reply, *J. Geophys. Res.*, *101*(B9), 20,137–20,140, 1996.

Atwater, T., and J. Stock, Pacific-North America plate tectonics of the Neogene southwestern United States: An update, *Int. Geol. Rev.*, *40*(5), 375–402, 1998.

Bakun, W. H., The seismogenic scaling factor, r, *U. S. Geol. Survey Open File Rep.*, *03-214*, B1–B9, 2003.

Beavan, J., P. Tregoning, M. Bevis, T. Kato, and C. Meertens, Motion and rigidity of the Pacific plate and implications for plate boundary deformation, *J. Geophys. Res.*, *107*(B10), doi:10.1029/2001JB000,282, 2002.

Behr, J., R. Bilham, P. Bodin, K. Breckenridge, and S. A.G, Increased surface creep rates on the San Andreas fault southeast of the Loma Prieta mainshock, in *Loma Prieta, California, earthquake of October 17, 1989: Aftershocks and postseismic effects*, edited by P. Reasonberg, U.S. Geological Survey Professional Paper 1550, pp. D179–D192, 1997.

Bennett, R. A., W. Rodi, and R. E. Reilinger, Global positioning system constraints on fault slip rates in southern California and northern Baja, Mexico, *J. Geophys. Res.*, *101*(B10), 21,943–21,960, 1996.

Bennett, R. A., J. L. Davis, and B. P. Wernicke, Present-day pattern of Cordilleran deformation in the western United States, *Geology*, *27*(4), 371–374, 1999.

Bennett, R. A., B. P. Wernicke, N. A. Niemi, A. M. Friedrich, and J. L. Davis, Contemporary strain rates in the northern Basin and Range province from GPS data, *Tectonics*, *22*(2, 1008), doi:10.1029/2001TC001,355, 2003.

Blanpied, M. L., D. A. Lockner, and J. D. Byerlee, Fault slip of granite at hydrothermal conditions, *J. Geophys. Res.*, *100*(B7), 1995.

Bryant, W., and S. Cluett, Fault number 52b, Ortigalita fault zone, Los Banos Valley section, in *Quaternary fault and fold database of the United States, ver 1.0*, U.S. Geological Survey Open File report 03-417, http://qfaults.cr.usgs.gov, 2000.

Bürgmann, R., P. Segall, M. Lisowski, and J. Svarc, Postseismic strain following the 1989 Loma Prieta earthquake from GPS and leveling measurements, *J. Geophys. Res.*, *102*(B3), 4933–4955, 1997.

Bürgmann, R., D. Schmidt, R. M. Nadeau, M. A. d'Alessio, E. Fielding, T. V. McEvilly, and M. H. Murray, Earthquake potential along the northern Hayward fault, California, *Science*, *289*(18 August 2000), 1178–1182, 2000.

Cox, A., and R. B. Hart, *Plate tectonics: How it works*, Blackwell Scientific Publications, Palo Alto, California, 1986.

d'Alessio, M. A., and S. J. Martel, Development of strike-slip faults from dikes, Sequoia National Park, California, *J. Struc. Geol.*, *in press*, 2004.

DeMets, C., and T. H. Dixon, New kinematic models for Pacific-North America motion from 3 Ma to present, I: Evidence for steady motion and biases in the NUVEL-1A model, *Geophys. Res. Lett.*, *26*(13), 1921–1924, 1999.

DeMets, C., R. G. Gordon, D. F. Argus, and S. Stein, Effect of recent revisions to the geomagnetic reversal time-scale on estimates of current plate motions, *Geophys. Res. Lett.*, *21*(20), 2191–2194, 1994.

Dixon, T. H., M. Miller, F. Farina, H. Z. Wang, and D. Johnson, Present-day motion of the Sierra Nevada block and some tectonic implications for the Basin and Range province, North American Cordillera, *Tectonics*, *19*(1), 1–24, 2000.

Freymueller, J. T., M. H. Murray, P. Segall, and D. Castillo, Kinematics of the Pacific-North America plate boundary zone, northern California, *J. Geophys. Res.*, *104*(B4), 7419–7441, 1999.

Fuis, G. S., and W. D. Mooney, Lithospheric structure and tectonics from seismic refraction and other data, in *The San Andreas fault system, California*, edited by R. E. Wallace, U.S. Geological Survey Professional Paper 1515, pp. 207–236, 1990.

Galehouse, J. S., and J. J. Lienkaemper, Inferences drawn from two decades of alinement array measurements of creep on faults in the San Francisco Bay Region, *Bull. Seism. Soc. Amer.*, *93*(6), 2415–2433, 2003.

Gilbert, L. E., C. H. Scholz, and J. Beavan, Strain localization along the San Andreas fault - consequences for loading mechanisms, *J. Geophys. Res.*, *99*(B12), 23,975–23,984, 1994.

Gonzalez-Garcia, J. J., L. Prawirodirdjo, Y. Bock, and D. Agnew, Guadalupe Island, Mexico as a new constraint for Pacific plate motion, *Geophys. Res. Lett.*, *30*(16), doi:10.1029/2003GL017,732, 2003.

Harris, R. A., and S. M. Day, Dynamic 3d simulations of earthquakes on en echelon faults, *Geophys. Res. Lett.*, *26*, 2089–2092, 1999.

Hearn, E. H., and E. D. Humphreys, Kinematics of the southern Walker Lane belt and motion of the Sierra Nevada block, California, *J. Geophys. Res.*, *103*(B11), 27,033–27,049, 1998.

Herring, T. A., GLOBK, global Kalman filter VLBI and GPS analysis program, 2002.

Jackson, J., Faulting, flow, and the strength of the continental lithosphere, *Int. Geol. Rev.*, *44*(1), 39–61, 2002.

Jennings, C., *Fault activity map of California and adjacent areas*, California Division of Mines and Geology, GDM 6, scale 1:750,000, 1994.

Johanson, I. A., and R. Bürgmann, Complexity at the junction of the Calaveras and San Andreas faults, *J. Geophys. Res.*, *in preparation*, 2004.

Kenner, S. J., and P. Segall, Postseismic deformation following the 1906 San Francisco earthquake, *J. Geophys. Res.*, *105*(B6), 13,195–13,209, 2000.

Kilb, D., and A. M. Rubin, Implications of diverse fault orientations imaged in relocated aftershocks of the Mount Lewis, M-L 5.7, California, earthquake, *J. Geophys. Res.*, *107*(B11), doi:10.1029/2001JB000,149, 2002.

King, R. W., and Y. Bock, Documentation for the GAMIT GPS analysis software, v.10.0, , Massachusetts Institute of Technology, Scripps Institute of Oceanography, 2002.

Kogan, M. G., G. M. Steblov, R. W. King, T. A. Herring, D. I. Frolov, S. G. Egorov, V. Y. Levin, A. Lerner-Lam, and A. Jones, Geodetic constraints on the rigidity and relative motion of Eurasia and North America, *Geophys. Res. Lett.*, *27*(14), 2041–2044, 2000.

Kreemer, C., W. E. Holt, and A. J. Haines, An integrated global model of present-day plate motions and plate boundary deformation, *Geophys. J. Int.*, *154*(1), 8–34, 2003.

Lachenbruch, A. H., and J. H. Sass, Heat flow and energetics of the San Andreas fault zone, *J. Geophys. Res.*, *85*(B11), 6185–6222, 1980.

Larson, K. M., J. T. Freymueller, and S. Philipsen, Global plate velocities from the Global Positioning System, *J. Geophys. Res.*, *102*(B5), 9961–9981, 1997.

Lienkaemper, J., J. Galehouse, and R. Simpson, Creep response of the Hayward fault to stress changes caused by the Loma Prieta earthquake, *Science*, *276*, 2014–2016, 1997.

Lienkaemper, J. J., J. S. Galehouse, and R. W. Simpson, Long-term monitoring of creep rate along the Hayward fault and evidence for a lasting creep response to 1989 Loma Prieta earthquake, *Geophys. Res. Lett.*, *28*(11), 2265–2268, 2001.

Linde, A. T., M. T. Gladwin, M. J. S. Johnston, R. L. Gwyther, and R. G. Bilham, A slow earthquake sequence on the San Andreas fault, *Nature*, *383*(6595), 65–68, 1996.

Magistrale, H., Relative contributions of crustal temperature and composition to controlling the depth of earthquakes in southern California, *Geophys. Res. Lett.*, *29*(10), 2002.

Malservisi, R., C. Gans, and K. P. Furlong, Numerical modeling of strike-slip creeping faults and implications for the Hayward fault, California, *Tectonophys.*, *361*(1-2), 121–137, 2003.

Manaker, D. M., R. Bürgmann, W. H. Prescott, and J. Langbein, Distribution of interseismic slip rates and the potential for significant earthquakes on the Calaveras fault, central California, *J. Geophys. Res.*, *108*(B6), doi:10.1029/2002JB001,749, 2003.

Matsu'ura, M., D. D. Jackson, and A. Cheng, Dislocation model for aseismic crustal deformation at Hollister, California, *J. Geophys. Res.*, *91*(B12), 2661–2674, 1986.

McCaffrey, R., Crustal block rotations and plate coupling, in *Plate boundary zones*, *AGU Geodynamics Series*, vol. 30, edited by S. Stein and J. T. Freymueller, pp. 101–122, 2002.

McClusky, S. C., S. C. Bjornstad, B. H. Hager, R. W. King, B. J. Meade, M. M. Miller, F. C. Monastero, and B. J. Souter, Present day kinematics of the Eastern California Shear Zone from a geodetically constrained block model, *Geophys. Res. Lett.*, *28*(17), 3369–3372, 2001.

Meade, B. J., and B. H. Hager, Block models of crustal motion in southern California constrained by GPS measurements, *J. Geophys. Res.*, *in review*, 2004.

Meade, B. J., B. H. Hager, S. McClusky, R. E. Reilinger, S. Ergintav, O. Lenk, A. Barka, and H. Ozener, Estimates of seismic potential in the Marmara Sea region from block models of secular deformation constrained by Global Positioning System measurements, *Bull. Seism. Soc. Amer.*, *92*, 208–215, 2002.

Miller, M. M., D. J. Johnson, C. M. Rubin, H. Dragert, K. Wang, A. Qamar, and C. Goldfinger, GPS-determination of along-strike variation in Cascadia margin kinematics: Implications for relative plate motion, subduction zone coupling, and permanent deformation, *Tectonics*, *20*(2), 161–176, 2001.

Murray, J. R., P. Segall, P. Cervelli, W. Prescott, and J. Svarc, Inversion of GPS data for spatially variable slip-rate on the San Andreas fault near Parkfield, CA, *Geophys. Res. Lett.*, *28*(2), 359–362, 2001.

Murray, M. H., and P. Segall, Modeling broadscale deformation in northern California and Nevada from plate motions and elastic strain accumulation, *Geophys. Res. Lett.*, *28*(22), 4315–4318, 2001.

Okada, Y., Surface deformation due to shear and tensile faults in a half-space, *Bull. Seism. Soc. Amer.*, *75*(4), 1135–1154, 1985.

Pollitz, F. F., and M. C. J. Nyst, A physical model for strain accumulation in the San Francisco Bay Region, *Geophys. J. Int.*, *in review*, 2004.

Prescott, W., D. Manaker, R. W. Simpson, and W. Ellsworth, R-factors inferred from geodetic modeling, *U. S. Geol. Survey Open File Rep.*, *03-214*, C1–C9, 2003.

Prescott, W. H., J. C. Savage, J. L. Svarc, and D. Manaker, Deformation across the Pacific-North America plate boundary near San Francisco, California, *J. Geophys. Res.*, *106*(B4), 6673–6682, 2001.

Reid, H. F., The mechanics of the earthquake, in *The California earthquake of April 18, 1906: Report of the State Investigation Commission*, vol. 2, Carnegie Institute of Washington, Washington, D.C., 1910.

Sauber, J., Geodetic measurement of deformation east of the San Andreas fault in central California, in *Slow deformation and transmission of stress in the Earth*, *Geophysical monograph*, vol. 49, edited by S. C. Cohen and P. Vanicek, pp. 71–86, American Geophysical Union, 1989.

Savage, J. C., Equivalent strike-slip earthquake cycles in half-space and lithosphere-asthenosphere Earth models, *J. Geophys. Res.*, *95*(B4), 4873–4879, 1990.

Savage, J. C., Viscoelastic-coupling model for the earthquake cycle driven from below, *J. Geophys. Res.*, *105*(B11), 25,525–25,532, 2000.

Savage, J. C., R. W. Simpson, and M. H. Murray, Strain accumulation rates in the San Francisco Bay Area, 1972-1989, *J. Geophys. Res.*, *103*(B8), 18,039–18,051, 1998.

Savage, J. C., J. L. Svarc, and W. H. Prescott, Geodetic estimates of fault slip rates in the San Francisco Bay Area, *J. Geophys. Res.*, *104*(B3), 4995–5002, 1999.

Savage, J. C., W. Gan, W. H. Prescott, and J. L. Svarc, Strain accumulation across the Coast Ranges at the latitude of San Francisco, 1994-2000, *J. Geophys. Res.*, *109*(B3), doi:10.1029/2003JB002,612, 2004.

Sawyer, T. L., and J. R. Unruh, Holocene slip rate constraints for the northern Greenville fault, eastern San Francisco Bay Area, California: Implications for the Mt. Diablo restraining stepover model, *EOS, Trans. Amer. Geophys. Union*, *83*(47), Abstract T62F–03, 2002.

Schmidt, D. A., R. Bürgmann, R. M. Nadeau, and M. A. d'Alessio, Distribution of aseismic slip-rate on the Hayward fault inferred from seismic and geodetic data, *J. Geophys. Res.*, *in review*, 2004.

Segall, P., Integrating geologic and geodetic estimates of slip rate on the San Andreas fault system, *Int. Geol. Rev.*, *44*(1), 62–82, 2002.

Segall, P., and R. Harris, Earthquake deformation cycle on the San Andreas fault near Parkfield, California, *J. Geophys. Res.*, *92*(B10), 10,511–10,525, 1987.

Segall, P., R. Bürgmann, and M. V. Matthews, Time dependent triggered afterslip following the 1989 Loma Prieta earthquake, *J. Geophys. Res.*, *105*, 5615–5634, 2000.

Sella, G. F., T. H. Dixon, and A. L. Mao, REVEL: A model for recent plate velocities from space geodesy, *J. Geophys. Res.*, *107*(B4), doi:10.1029/2000JB000,033, 2002.

Shen, Z.-K., et al., Southern California Earthquake Center Crustal Motion Map Version 3.0, http://epicenter.usc.edu/cmm3/, 2003.

Sibson, R. H., Fault zone models, heat flow, and the depth distribution of earthquakes in the continental crust of the United States, *Bull. Seism. Soc. Amer.*, *68*, 1421–1448, 1982.

Simpson, R. W., J. J. Lienkaemper, and J. S. Galehouse, Variations in creep rate along the Hayward fault, California, interpreted as changes in depth of creep, *Geophys. Res. Lett.*, *28*(11), 2269–2272, 2001.

Steblov, G. M., M. G. Kogan, R. W. King, C. H. Scholz, R. Bürgmann, and D. I. Frolov, Imprint of the North American plate in Siberia revealed by GPS, *Geophys. Res. Lett.*, *30*(18), doi:10.1029/2003GL017,805, 2003.

Thatcher, W., Strain accumulation on northern San Andreas fault zone since 1906, *J. Geophys. Res.*, *80*(35), 4873–4880, 1975.

Thatcher, W., G. Marshall, and M. Lisowski, Resolution of fault slip along the 470-km-long rupture of the great 1906 San Francisco earthquake and its implications, *J. Geophys. Res.*, *102*(B3), 5353–5367, 1997.

Thatcher, W., G. R. Foulger, B. R. Julian, J. Svarc, E. Quilty, and G. W. Bawden, Present-day deformation across the Basin and Range province, western United States, *Science*, *283*, 1714–1718, 1999.

Townend, J., and M. D. Zoback, Focal mechanism stress inversions in southern California and the strength of the San Andreas fault, in *Proceedings of the Conference on Tectonic Problems of the San Andreas Fault System*, vol. 30, pp. 268–276, Stanford University Publication, Geological Sciences, 2001.

Tse, S. T., and J. R. Rice, Crustal instability in relation to the depth variation of frictional slip properties, *J. Geophys. Res.*, *91*(B9), 9452–9472, 1986.

Unruh, J. R., and W. R. Lettis, Kinematics of transpressional deformation in the eastern San Francisco Bay region, California, *Geology*, *26*, 19–22, 1998.

Unruh, J. R., and T. L. Sawyer, Assessment of blind seismogenic sources, Livermore Valley, eastern San Francisco Bay Region: Final technical report submitted to the U.S. Geological Survey, National Earthquake Hazards Reduction Program, award no. 1434-95-g-2611, 1997.

Unruh, J. R., and T. L. Sawyer, Paleoseismic investigation of the northern Greenville fault, eastern San Francisco Bay Area, California: Final technical report submitted to the U.S. Geological Survey, National Earthquake Hazards Reduction Program award no. 1434-hq-97-gr-03146, , 1998.

Unruh, J. R., K. I. Kelson, D. Manaker, and A. Barron, Critical evaluation of the northern termination of the Calaveras fault, eastern San Francisco Bay Area, California, *Report 1430*, William Lettis and Associates, 2002.

Wakabayashi, J., Distribution of displacement on and evolution of a young transform system: The northern San Andreas fault system, California, *J. Geophys. Res.*, *18*(B6), 1245–1274, 1999.

Waldhauser, F., and W. L. Ellsworth, Fault structure and mechanics of the Hayward fault, California, from double-difference earthquake locations, *J. Geophys. Res.*, *107*(B3), doi:10.129/2000JB000,084, 2002.

Wentworth, C. M., and M. D. Zoback, The style of late Cenozoic deformation at the eastern-front of the California Coast Ranges, *Tectonics*, *8*(2), 237–246, 1989.

Wentworth, C. M., and M. D. Zoback, The style of the late Cenozoic deformation at the eastern-front of the California Coast Ranges - reply, *Tectonics*, *9*(5), 1267–1268, 1990.

Wernicke, B., and J. K. Snow, Cenozoic tectonism in the central Basin and Range: Motion of the Sierran-Great Valley block, *Int. Geol. Rev.*, *40*(5), 403–410, 1998.

Wesnousky, S. G., Crustal deformation processes and the stability of the Gutenberg-Richter relationship, *Bull. Seism. Soc. Amer.*, *89*(4), 1131–1137, 1999.

Williams, C. F., Temperature and the seismic/aseismic transition: Observations from the 1992 Landers earthquake, *Geophys. Res. Lett.*, *23*(16), 2029–2032, 1996.

Williams, C. F., Implications of the depth of seismicity for the rupture extent of future earthquakes in the San Francisco Bay Area, *U. S. Geol. Survey Open File Rep.*, *03-214*, A1–A16, 2003.

Wong, I. G., and R. W. Ely, Historical seismicity and tectonics of the Coast Ranges-Sierra block boundary: Implications to the 1983 Coalinga earthquakes, in *The 1983 Coalinga, California earthquakes*, edited by J. Bennet and R. Sherburne, California Division of Mines and Geology Special Publication 66, pp. 89–104, 1983.

Working Group on Northern California Earthquake Probabilities, Earthquake probabilities in the San Francisco Bay region: 2002 to 2031, *U.S. Geol. Surv. Open File Rep.*, *03-214*, 2003.

Yu, E., and P. Segall, Slip in the 1868 Hayward earthquake from the analysis of historical triangulation data, *J. Geophys. Res.*, *101*(B7), 16,101–16,118, 1996.